ASTRONOMY & ASTROPHYSICS
SUPPLEMENT SERIES

JUNE 1987, PAGE 345

Astron. Astrophys. Suppl. Ser. **69**, 345-370 (1987)

Effects of dust on the formation of lines in an expanding spherical medium

A. Peraiah, B. A. Varghese and M. S. Rao

Indian Institute of Astrophysics, Bangalore 560034, India

Received May 6, accepted December 22, 1986

Summary. — We have computed a series of line profiles formed in a spherically symmetric and radially expanding atmosphere in which dust is present. We assumed that the dust scatters radiation isotropically. Two cases of dust distribution are employed : (1) uniform distribution of dust through out the medium and (2) density increasing with radius. The density and the velocity of expansion of the gaseous component are assumed to satisfy the equation of continuity. We assumed a model of two-level atom in non-LTE approximation with complete redistribution. The calculations are done in the comoving frame of the fluid and later transformed to a point at infinity.

Key words : expanding atmospheres — dust — comoving frame, line profiles.

1. Introduction.

The presence of dust is revealed in the infrared observations of many objects such as gaseous nebulae, active galactic nuclei, T Tauri stars, and atmospheres of cool supergiants. Allen (1973) studied 248 early type emission line stars and related objects and found that two mechanisms, viz. free-free radiation and thermal emission from dust grains, are probably active in producing the observed infrared excess. Stars with prominent infrared continua are found to have circumstellar envelopes (Geisel, 1970 ; Allen and Swings, 1972). Schwartz *et al.* (1983) investigated the far infrared and submillimeter mapping of S140 IRS and found that there is good coupling between dust and gas. Grasdalen (1976) discovered Brα line radiation from Beckline-Neugebauer (BN) object in Orion. It is found from an extensive survey of such objects that many show the presence of ionized gas. Some of these objects (e.g. BN and CRL 490) appear to possess a dusty shell around a hard core of ionized gas (Simon *et al.*, 1981). Simon *et al.* (1985) observed Brγ, Pfγ and Brα IR lines of compact molecular clouds. Based upon infrared photometric observations from 2.3 μm to 10 μm, Persi *et al.* (1983) derived mass loss rates for 15 Of-type stars. Huggins *et al.* (1984) studied abundances in the envelope of IRC + 10216 through the line analysis. They have adopted the approach followed by Kwan and Hill (1977) and Henkel *et al.* (1983). Felli (1982) studied the infrared emission from extended stellar envelope. The study of line formation in the dusty envelopes remains practically unexplored.

Presence of dust, radial expansion, geometrical extension, chemical composition etc. are some of the physical and geometrical properties we must include in the calculations of the line formation. Recently there have been few attempts to study the radiative transfer effects in a medium which contains both dust and gas (see Hummer and Kunasz, 1980 ; and Wehrse and Kalkofen, 1985). Peraiah and Wehrse (1978) and Wehrse and Peraiah (1979) studied the effects of radial expansion in the rest frame in which small velocities of the order of 2 mean thermal Doppler units were used. In the present work, we have used velocities as large as 20 Doppler units. The calculations have been performed initially in the comoving frame. Subsequently the transformation is carried for a point at infinity.

In this paper we present results from our comoving frame calculations assuming an envelope containing a mixture of gas and dust which is expanding radially. In section 2 we shall present a brief outline of the method of computations of the lines. The results are discussed in section 3 followed by conclusion in section 4.

2. A brief description of the method of solution for line transfer in comoving frame.

In spherical geometry the terms that should be included in the transfer equation when it is transformed into the

comoving frame are given by (see Chandrasekhar, 1945 ; Mihalas *et al.*, 1975 ; Mihalas, 1978) :

$$\left\{(1-\mu^2)\frac{V(r)}{r}+\mu^2\frac{dV(r)}{dr}\right\}\frac{\partial I(r,\mu,x)}{\partial x}, \quad (1)$$

where $I(r, \mu, x)$ is the specific intensity of the ray with standardized frequency x ($= (\nu - \nu_0)/\Delta$, Δ being mean thermal Doppler unit and ν_0 and ν being the frequencies at line centre and at any point in the line respectively) making an angle $\cos^{-1}\mu$ with the radial vector of point r. $V(r)$ is the radial velocity of the gas at r in mean thermal Doppler units (mtu). We shall now write the equation of line transfer in the comoving frame with absorption and emission due to dust and gas. This is given by (see Peraiah and Wehrse, 1978 ; Peraiah, 1984, Wehrse and Kalkofen, 1985),

$$\mu\frac{\partial I(r,\mu,x)}{\partial r}+\frac{1-\mu^2}{r}\frac{\partial I(r,\mu,x)}{\partial\mu}= = K_L(r)[(\phi(x)+\beta)][S(r,\mu,x)-I(r,\mu,x)] + \left\{(1-\mu^2)\frac{V(r)}{r}+\mu^2\frac{dV(r)}{dr}\right\}\frac{\partial I(r,\mu,x)}{\partial x} + K_{dust}(r)\{S_{dust}(r,\mu,x)-I(r,\mu,x)\}. \quad (2)$$

For the oppositely directed beam, we have,

$$-\mu\frac{\partial I(r,-\mu,x)}{\partial\mu}-\frac{1-\mu^2}{r}\frac{\partial I(r,-\mu,x)}{\partial\mu}= = K_L(r)[\phi(x)+\beta][S(r,-\mu,x)-I(r,-\mu,x)] + \left\{(1-\mu^2)\frac{V(r)}{r}+\mu^2\frac{dV(r)}{dr}\right\}\frac{\partial I(r,-\mu,x)}{\partial x} + K_{dust}(r)\{S_{dust}(r,-\mu,x)-I(r,-\mu,x)\}, \quad (3)$$

where $\mu \in (0, 1)$. Here $K_L(r)$ is absorption coefficient at the line centre, $\phi(x)$ the Doppler profile function. β is the ratio of continuum to line opacities. The quantity $S(r, \pm\mu, x)$ is the source function given by :

$$S(r,\pm\mu,x)=\frac{\phi(x)}{\phi(x)+\beta}S_L(r)+\frac{\beta}{\phi(x)+\beta}S_C(r,x) \quad (4)$$

and

$$S_L(r)=\frac{1}{2}(1-\varepsilon)\int_{-\infty}^{+\infty}\phi(x)\int_{-1}^{+1}I(r,\mu',x)\,dx\,d\mu' + + \varepsilon B(T(r),x). \quad (5)$$

is the line source function. The quantity $S_C(r)$ is the continuum source function given by :

$$S_C(r)=\rho(r)\,B(T(r),x). \quad (6)$$

Here ε is the probability per each scattering that a photon will be destroyed by collisional de-excitation. $B(T(r), x)$ is the Planck function and $\rho(r)$ is an arbitrary quantity. $K_{dust}(r)$ is the absorption coefficient of the dust whose source function $S_{dust}(r, \pm\mu, x)$ is given by :

$$S_{dust}(r,\pm\mu,x)=(1-\omega)B_{dust}+ + \frac{\omega}{2}\int_{-\infty}^{+\infty}P(\mu,\mu',r)\,I(r,\mu',x)\,d\mu' \quad (7)$$

where B_{dust} is the Planck function for the dust emission, ω the albedo of the dust and P the scattering phase function. It is assumed that isotropic and coherent scattering holds. The quantity B_{dust} is normally neglected because the re-emission will be far away from the line centre and therefore may not contribute to the line radiation. Although we need not consider the term containing B_{dust}, we have included it for the sake of completeness.

We have adopted the « CELL » method described by Peraiah (1984) to solve equations (2) and (3). This is done by a suitable discretization in frequency, angle as well as radius. For frequency discretization we choose the discrete points x_i and weights a_i such that :

$$\int_{-\infty}^{+\infty}\phi(x)\,f(x)\,dx\simeq\sum_{i=-I}^{I}a_i\,f(x), \qquad \sum_{i=-I}^{I}a_i=1. \quad (8)$$

The angle discretization is done with abscissae $\{\mu_j\}$ and weights $\{C_j\}$ such that :

$$\int_0^1 f(x)\,d\mu\simeq\sum_{j=1}^{m}C_j\,f(\mu_j),\ \sum_{j=1}^{m}C_j=1 \quad (9)$$

We choose the radial points r_n and r_{n+1} as discrete points for radial discretization. The integration of equations (2) and (3) is done on the « CELL » bounded by :

$$[r_n, r_{n+1}][\mu_{j-1/2}, \mu_{j+1/2}][x_i, x_{i+1}].$$

The quantities $\mu_{j+1/2}$ are chosen according to convenience. In this problem we choose $\mu_{j+1/2}$ by the relation,

$$\mu_{j+1/2}=\sum_{k=1}^{j}C_k, \qquad j=1,2,\ldots,m. \quad (10)$$

We have chosen μ's and C's to be roots and weights of Gauss-Legendre quadrature. We shall write the following m vectors,

$$\mathbf{h}=[1,1,\ldots,1]^T, \quad (11)$$

where T indicates transpose. Let us introduce :

$$\mathbf{U}^+_{i,n}=4\pi r_n^2\begin{bmatrix}I(\mu_1,x_i,\tau_n)\\ I(\mu_2,x_i,\tau_n)\\ \vdots\\ I(\mu_m,x_i,\tau_n)\end{bmatrix}, \quad (12)$$

$$\mathbf{U}^-_{i,n} = 4\,\pi r_n^2 \begin{bmatrix} I(-\mu_1, x_i, \tau_n) \\ I(-\mu_2, x_i, \tau_n) \\ \vdots \\ I(-\mu_m, x_i, \tau_n) \end{bmatrix}, \qquad (13)$$

and

$$B'(\nu_0, T_e(r)) = 4\,\pi r_n^2\, B(\nu_0, T_e(r))\,. \qquad (14)$$

After integration equations (2) and (3) reduce to :

$$\mathbf{M}_m(\mathbf{U}^+_{i,n+1} - \mathbf{U}^+_{i,n}) + \rho_c(\Lambda^+_m\,\mathbf{U}^+_{i,n+1/2} + \Lambda^-_m\,\mathbf{U}^-_{i,n+1/2}) +$$
$$+ \tau_{g,n+1/2}(\beta + \phi_i)_{n+1/2}\,\mathbf{U}^+_{i,n+1/2} + \tau_{d,n+1/2}\,\mathbf{U}^+_{i,n+1/2} = \tau_{g,n+1/2}(\rho\beta + \varepsilon\phi_i)_{n+1/2}\,B'^{,+}_{g,n+1/2}\,\mathbf{h}$$
$$+ \frac{1}{2}\,\tau_{g,n+1/2}\,\sigma_{n+1/2}\,\phi_{i,n+1/2} \sum_{i'=-I}^{I} a_{i',n+1/2}(\mathbf{h}\mathbf{h}^{\mathrm{T}})\,\mathbf{C}_m(\mathbf{U}^+ + \mathbf{U}^-)_{i',n+1/2}$$
$$+ \frac{1}{2}\,\tau_{d,n+1/2}\,\omega_{n+1/2}(\mathbf{P}^{++}_{m,n+1/2}\,C_m\,\mathbf{U}^+_{i,n+1/2} + \mathbf{P}^{+-}_{m,n+1/2}\,\mathbf{C}_m\,\mathbf{U}^-_{i,n+1/2})$$
$$+ \mathbf{M}_{1,i+1/2}\,\mathbf{d}_{i+1/2}\,\mathbf{U}^+_{i+1/2,n+1/2} + \tau_{d,n+1/2}(1-\omega)_{n+1/2}\,B'^{,+}_{d,n+1/2}\,\mathbf{h} \qquad (15)$$

and

$$\mathbf{M}_m(\mathbf{U}^-_{i,n} - \mathbf{U}^-_{i,n+1}) - \rho_c(\Lambda^+_m\,\mathbf{U}^-_{i,n+1/2} + \Lambda^-_m\,\mathbf{U}^+_{i,n+1/2}) +$$
$$+ \tau_{g,n+1/2}(\beta + \phi_i)_{n+1/2}\,\mathbf{U}^-_{i,n+1/2} + \tau_{d,n+1/2}\,\mathbf{U}^-_{i,n+1/2} = \tau_{g,n+1/2}(\rho\beta + \varepsilon\phi_i)_{n+1/2}\,B^{i,+}_{g,n+1/2}\,\mathbf{h}$$
$$+ \frac{1}{2}\,\tau_{g,n+1/2}\,\sigma_{n+1/2}\,\phi_{i,n+1/2} \sum_{i'=-I}^{I} a_{i',n+1/2}(\mathbf{h}\mathbf{h}^{\mathrm{T}})\,\mathbf{C}_m(\mathbf{U}^+ + \mathbf{U}^-)_{i',n+1/2}$$
$$+ \frac{1}{2}\,\tau_{d,n+1/2}\,\omega_{n+1/2}(\mathbf{P}^{-+}_{m,n+1/2}\mathbf{C}_m\,\mathbf{U}^+_{i,n+1/2} + \mathbf{P}^{--}_{m,n+1/2}\,\mathbf{C}_m\,\mathbf{U}^-_{i,n+1/2})$$
$$+ \mathbf{M}_{1,i+1/2}\,\mathbf{d}_{i+1/2}\,\mathbf{U}^-_{i+1/2,n+1/2} + \tau_{d,n+1/2}(1-\omega)_{n+1/2}\,B'^{,+}_{d}\,\mathbf{h}\,, \qquad (16)$$

where :

$$\mathbf{M}_m = [\mu_j\,\delta_{jk}]\,, \quad \mathbf{C}_m = [C_j\,\delta_{jk}] \qquad (17)$$

and

$$d_{i+1/2} = (x_{i+1} - x_i)^{-1}\,, \quad \mathbf{U}^{\pm}_{i+1/2} = \frac{1}{2}\,(\mathbf{U}^{\pm}_i + \mathbf{U}^{\pm}_{i+1})\,. \qquad (18)$$

The subscript $n + 1/2$ corresponds to the average of the quantity over the « CELL » bounded by r_n and r_{n+1}. The quantities Λ^+_m and Λ^-_m are the curvature matrices (see Peraiah, 1984), and :

$$M_{1,i+1/2} = M_{i+1/2}\,\Delta V_{n+1/2} + M_{i+1/2}\,\rho_c\,V_{n+1/2}\,, \qquad (19)$$

$$M^1_{i+1/2} = [\mu_j^2\,\delta_{jk}]\,, \quad M^2_{i+1/2} = [(1-\mu_j^2)\,\delta_{jk}]\,, \qquad (20)$$

with

$$\Delta V_{n+1/2} = V_{n+1} - V_n\,.$$

Furthermore, we have,

$$\tau_{n+1/2} = K_{\mathrm{gas}}\,.\,\Delta r\,, \quad \tau_{d,n+1/2} = K_{\mathrm{dust}}\,.\,\Delta r \qquad (21)$$

and

$$\sigma_{n+1/2} = 1 - \varepsilon_{n+1/2}\,.$$

The quantity ρ_c is called the curvature factor given by :

$$\rho_c = \Delta r / r_{n+1/2}\,. \qquad (22)$$

The matrices P^{++}, P^{+-}, P^{-+}, P^{--} are the phase matrices of dimension m and for isotropic scattering, all the elements of these matrices are equal to unity.

Equations (15) and (16) are rewritten for I frequency points as follows :

$$\mathbf{M}(\mathbf{U}^+_{n+1} - \mathbf{U}^+_n) + \rho_c(\Lambda^+\,\mathbf{U}^+_{n+1/2} + \Lambda^-\,\mathbf{U}^-_{n+1/2}) +$$
$$+ \tau_{g,n+1/2}\,\mathbf{\Phi}_{n+1/2}\,\mathbf{U}^+_{n+1/2} + \tau_{d,n+1/2}\,\mathbf{E}\mathbf{U}^+_{n+1/2} = \tau_{g,n+1/2}\,\mathbf{S}^+_{n+1/2} + \frac{1}{2}\,\tau_{g,n+1/2}\,\sigma_{n+1/2}(\mathbf{\Phi}\mathbf{\Phi}^{\mathrm{T}}\,\mathbf{W})(\mathbf{U}^+ + \mathbf{U}^-)_{n+1/2}$$
$$+ \frac{1}{2}\,\tau_{d,n+1/2}\,\omega_{n+1/2}(\mathbf{P}^{++}\,\mathbf{C}\mathbf{U}^+ + \mathbf{P}^{+-}\,\mathbf{C}\mathbf{U}^-)_{n+1/2} + \tau_{d,n+1/2}(1-\omega_{n+1/2})\,\mathbf{B}'^{,+}_{d,n+1/2} + \mathbf{M}_1\,\mathbf{d}\mathbf{U}^+_{n+1/2}\,, \qquad (23)$$

and

$$\mathbf{M}(\mathbf{U}_n^- - \mathbf{U}_{n+1}^-) - \rho_c(\mathbf{\Lambda}^+ \mathbf{U}_{n+1/2}^- + \mathbf{\Lambda}^- \mathbf{U}_{n+1/2}^+) +$$

$$+ \tau_{g,n+1/2} \mathbf{\Phi}_{n+1/2} \mathbf{U}_{n+1/2}^- + \tau_{d,n+1/2} \mathbf{E}\mathbf{U}_{n+1/2}^- = \tau_{g,n+1/2} \mathbf{S}_{n+1/2}^- + \frac{1}{2} \tau_{g,n+1/2} \sigma_{n+1/2} (\mathbf{\Phi}\mathbf{\Phi}^{\mathrm{T}} \mathbf{W})(\mathbf{U}^+ + \mathbf{U}^-)_{n+1/2}$$

$$+ \frac{1}{2} \tau_{d,n+1/2} \omega_{n+1/2} (\mathbf{P}^{-+} \mathbf{C}\mathbf{U}^+ + \mathbf{P}^{--} \mathbf{C}\mathbf{U}^-)_{n+1/2} + \tau_{d,n+1/2}(1 - \omega_{n+1/2}) \mathbf{B}'^-_{d,n+1/2} + \mathbf{M}_1 \mathbf{d}\mathbf{U}^-_{n+1/2}, \quad (24)$$

where

$$\mathbf{U}_N^{\pm} = [\mathbf{U}_{1,n}^{\pm}, \mathbf{U}_{i,n}^{\pm}, \ldots, \mathbf{U}_{I,n}^{\pm}]^{\mathrm{T}}, \quad (25)$$

$$\mathbf{M} = \begin{bmatrix} \mathbf{M}_m & & & \\ & \mathbf{M}_m & & \\ & & \ddots & \\ & & & \mathbf{M}_m \end{bmatrix}, \quad \mathbf{C} = \begin{bmatrix} \mathbf{C}_m & & & \\ & \mathbf{C}_m & & \\ & & \ddots & \\ & & & \mathbf{C}_m \end{bmatrix},$$

$$\mathbf{\Phi}_{n+1/2} = [\Phi_{kk'}]_{n+1/2} = (\beta + \phi_k)_{n+1/2} \delta_{kk'}$$

$$k = j + (i-1)m \quad 1 \leqslant k \leqslant K = mI$$

i, j being the running indices of frequency and angle discretization, and :

$$S^+_{n+1/2} = (\rho\beta + \varepsilon\phi_k) B'^+_{n+1/2} \delta_{kk'}$$

$$\phi_i W_k = A_i C_j \quad \text{where} \quad A_i = \frac{a_i \phi_i}{\sum_{i'=-I}^{I} A_i \phi(x_i)}.$$

E is the unit matrix of $K \times K$ dimensions. The quantities P^{++} etc. are given by :

$$\mathbf{P}^{++} = \begin{bmatrix} \mathbf{P}_m^{++} & & & \\ & \mathbf{P}_m^{++} & & \\ & & \ddots & \\ & & & \mathbf{P}_m^{++} \end{bmatrix}. \quad (26)$$

For isotropic scattering P^{++}, P^{+-} etc. are all equal. Furthermore,

$$\mathbf{B}'^{\pm}_{d,n+1/2} = B'^{\pm}_{d,n+1/2} \mathbf{h}, \quad (27)$$

$$\mathbf{M}_1 = [\mathbf{M}^1 \Delta V_{n+1/2} + \mathbf{M}^2 \rho_c V_{n+1/2}], \quad (28)$$

$$\mathbf{M}^1 = \begin{bmatrix} \mathbf{M}_m^1 & & \\ & \ddots & \\ & & \mathbf{M}_m^1 \end{bmatrix}, \quad \mathbf{M}_m^1 = [\mu_j^2 \delta_{jl}], \quad (29)$$

$$\mathbf{M}^2 = \begin{bmatrix} \mathbf{M}_m^2 & & \\ & \ddots & \\ & & \mathbf{M}_m^2 \end{bmatrix}, \quad \mathbf{M}_m^2 = [(1 - \mu_j^2) \delta_{jl}] \quad (30)$$

$j, l = 1, 2, \ldots, m.$

and :

$$\mathbf{d} = \begin{bmatrix} -d_1 & d_1 & 0 & & & \\ -d_2 & 0 & d_2 & & & \\ 0 & -d_3 & 0 & d_3 & & \\ & \ddots & \ddots & \ddots & \ddots & \\ & & & & d_{I-1} & \\ & & & -d_I & d_I & \end{bmatrix} \quad (31)$$

where

$$d_i = (x_{i+1} - x_{i-1})^{-1}, \quad i = 2, 3, \ldots, I-1. \quad (32)$$

We replace $\mathbf{U}^+_{n+1/2}$, $\mathbf{U}^-_{n+1/2}$ by the diamond scheme given by,

$$\mathbf{U}^+_{n+1/2} = \frac{1}{2}(\mathbf{U}^+_n + \mathbf{U}^+_{n+1}),$$
$$\mathbf{U}^-_{n+1/2} = \frac{1}{2}(\mathbf{U}^-_n + \mathbf{U}^-_{n+1}), \quad (33)$$

Substitution of equations (33) into equations (23) and (24) will give us :

$$\begin{bmatrix} \mathbf{M} + \frac{1}{2}\rho_c \mathbf{\Lambda}^+ + \frac{1}{2}\tau_g\left(\mathbf{\Phi} - \frac{1}{2}\sigma\mathbf{\phi}\mathbf{\phi}^{\mathrm{T}}\mathbf{W}\right) + \frac{1}{2}\tau_d\left(\mathbf{E} - \frac{1}{2}\omega\mathbf{P}^{++}\mathbf{C}\right) - \frac{1}{2}\mathbf{M}_1\mathbf{d} - & \frac{1}{2}\rho_c\mathbf{\Lambda}^- - \frac{1}{4}\tau_g\sigma(\mathbf{\phi}\mathbf{\phi}^{\mathrm{T}}\mathbf{W}) - \frac{1}{4}\tau_d\omega\mathbf{P}^{+-}\mathbf{C} \\ -\frac{1}{2}\rho_c\mathbf{\Lambda}^- - \frac{1}{4}\tau_g\sigma(\mathbf{\phi}\mathbf{\phi}^{\mathrm{T}}\mathbf{W}) - \frac{1}{4}\tau_d\mathbf{P}^{-+}\mathbf{C} & \mathbf{M} - \frac{1}{2}\rho_c\mathbf{\Lambda}^+ + \frac{1}{2}\tau_g\left(\mathbf{\Phi} - \frac{1}{2}\sigma\mathbf{\phi}\mathbf{\phi}^{\mathrm{T}}\mathbf{W}\right) + \frac{1}{2}\tau_d\left(\mathbf{E} - \frac{1}{2}\omega\mathbf{P}^{--}\mathbf{C}\right) - \frac{1}{2}\mathbf{M}_1\mathbf{d} \end{bmatrix} \begin{bmatrix} \mathbf{U}^+_{n+1} \\ \mathbf{U}^-_n \end{bmatrix}$$

$$= \begin{bmatrix} \mathbf{M} - \frac{1}{2}\rho_c \mathbf{\Lambda}^+ - \frac{1}{2}\tau_g\left(\mathbf{\Phi} - \frac{1}{2}\sigma\boldsymbol{\phi}\boldsymbol{\phi}^{\mathrm{T}}\mathbf{W}\right) - \frac{1}{2}\tau_d\left(\mathbf{E} - \frac{1}{2}\omega\mathbf{P}^{++}\mathbf{C}\right) + \frac{1}{2}\mathbf{M}_1\mathbf{d} & \\ \frac{1}{2}\rho_c \mathbf{\Lambda}^- + \frac{1}{4}\tau_g\sigma(\boldsymbol{\phi}\boldsymbol{\phi}^{\mathrm{T}}\mathbf{W}) + \frac{1}{4}\tau_d\omega\mathbf{P}^{-+}\mathbf{C} & \end{bmatrix}$$

$$\begin{bmatrix} -\frac{1}{2}\rho_c \mathbf{\Lambda}^- + \frac{1}{4}\tau_g\sigma(\boldsymbol{\phi}\boldsymbol{\phi}^{\mathrm{T}}\mathbf{W}) + \frac{1}{4}\tau_d\omega\mathbf{P}^{+-}\mathbf{C} & \\ \mathbf{M} + \frac{1}{2}\rho_c \mathbf{\Lambda}^+ - \frac{1}{2}\tau_g\left(\mathbf{\Phi} - \frac{1}{2}\sigma\boldsymbol{\phi}\boldsymbol{\phi}^{\mathrm{T}}\mathbf{W}\right) - \frac{1}{2}\tau_d\left(\mathbf{E} - \frac{1}{2}\omega\mathbf{P}^{--}\mathbf{C}\right) + \frac{1}{2}\mathbf{M}_1\mathbf{d} & \end{bmatrix} \begin{bmatrix} \mathbf{U}_n^+ \\ \mathbf{U}_{n+1}^- \end{bmatrix}$$

$$+ \tau_g \begin{bmatrix} \mathbf{S}^+ \\ \mathbf{S}^- \end{bmatrix} + \tau_d(1-\omega)\begin{bmatrix} \mathbf{B}'^{,+} \\ \mathbf{B}'^{,-} \end{bmatrix}, \tag{34}$$

where E is the unit matrix. Let us define the following quantities:

$$\mathbf{Z}^{++} = \left(\mathbf{\Phi} - \frac{1}{2}\sigma\boldsymbol{\phi}\boldsymbol{\phi}^{\mathrm{T}}\mathbf{W}\right) + \frac{\tau_d}{\tau_g}\left(\mathbf{E} - \frac{1}{2}\omega\mathbf{P}^{++}\mathbf{C}\right) - \frac{\mathbf{M}_1\mathbf{d}}{\tau_g} + \frac{\rho_c\mathbf{\Lambda}^+}{\tau_g}, \tag{35}$$

$$\mathbf{Z}^{--} = \left(\mathbf{\Phi} - \frac{1}{2}\sigma\boldsymbol{\phi}\boldsymbol{\phi}^{\mathrm{T}}\mathbf{W}\right) + \frac{\tau_d}{\tau_g}\left(\mathbf{E} - \frac{1}{2}\omega\mathbf{P}^{--}\mathbf{C}\right) - \frac{\mathbf{M}_1\mathbf{d}}{\tau_g} - \frac{\rho_c\mathbf{\Lambda}^+}{\tau_g}, \tag{36}$$

$$\mathbf{\Delta}^+ = \left(\mathbf{M} + \frac{1}{2}\tau_g\mathbf{Z}^{++}\right)^{-1}, \quad \mathbf{\Delta}^- = \left(\mathbf{M} + \frac{1}{2}\tau_g\mathbf{Z}^{--}\right)^{-1}, \tag{37}$$

$$\mathbf{Y}^{+-} = \frac{1}{2}\sigma\boldsymbol{\phi}\boldsymbol{\phi}^{\mathrm{T}}\mathbf{W} + \frac{1}{2}\frac{\tau_d}{\tau_g}\omega\mathbf{P}^{+-}\mathbf{C} - \frac{\rho_c\mathbf{\Lambda}^-}{\tau_g}, \tag{38}$$

$$\mathbf{Y}^{-+} = \frac{1}{2}\sigma\boldsymbol{\phi}\boldsymbol{\phi}^{\mathrm{T}}\mathbf{W} + \frac{1}{2}\frac{\tau_d}{\tau_g}\omega\mathbf{P}^{-+}\mathbf{C} + \frac{\rho_c\mathbf{\Lambda}^-}{\tau_g}, \tag{39}$$

$$\mathbf{A} = \mathbf{M} - \frac{1}{2}\tau_g\mathbf{Z}^{++}, \quad \mathbf{D} = \mathbf{M} - \frac{1}{2}\tau_g\mathbf{Z}^{--}, \tag{40}$$

$$\mathbf{g}^{+-} = \frac{1}{2}\tau_g\mathbf{\Delta}^+\mathbf{Y}^{+-}, \quad \mathbf{g}^{-+} = \frac{1}{2}\tau_g\mathbf{\Delta}^-\mathbf{Y}^{-+}, \tag{41}$$

$$\mathbf{G}^{+-} = [\mathbf{E} - \mathbf{g}^{+-}\mathbf{g}^{-+}]^{-1}, \quad \mathbf{G}^{-+} = [\mathbf{E} - \mathbf{g}^{-+}\mathbf{g}^{+-}]^{-1}, \tag{42}$$

$$\mathbf{S}_1^+ = \mathbf{S}^+ + \frac{\tau_d}{\tau_g}(1-\omega)\mathbf{B}_d'^{+}, \tag{43}$$

$$\mathbf{S}_1^- = \mathbf{S}^- + \frac{\tau_d}{\tau_g}(1-\omega)\mathbf{B}_d'^{-}. \tag{44}$$

Using equations (35) to (44) we can write the reflection and transmission matrices. These are given by,

$$\mathbf{t}(n+1, n) = \mathbf{G}^{+-}(\mathbf{\Delta}^+\mathbf{A} + \mathbf{g}^{+-}\mathbf{g}^{-+}), \tag{45}$$

$$\mathbf{t}(n, n+1) = \mathbf{G}^{-+}(\mathbf{\Delta}^-\mathbf{D} + \mathbf{g}^{-+}\mathbf{g}^{+-}), \tag{46}$$

$$\mathbf{r}(n+1, n) = \mathbf{G}^{-+}\mathbf{g}^{-+}(\mathbf{E} + \mathbf{\Delta}^+\mathbf{A}), \tag{47}$$

and

$$\mathbf{r}(n, n+1) = \mathbf{G}^{+-}\mathbf{g}^{+-}(\mathbf{E} + \mathbf{\Delta}^-\mathbf{D}). \tag{48}$$

The related source vectors are given by:

$$\mathbf{\Sigma}^+ = \tau_g\mathbf{G}^{+-}(\mathbf{\Delta}^+\mathbf{S}_1^+ + \mathbf{g}^{+-}\mathbf{\Delta}^-\mathbf{S}_1^-), \tag{49}$$

and

$$\mathbf{\Sigma}^- = \tau_g\mathbf{G}^{-+}(\mathbf{\Delta}^-\mathbf{S}_1^- + \mathbf{g}^{-+}\mathbf{\Delta}^+\mathbf{S}_1^+). \tag{50}$$

The transmission and reflection operators and the source vectors which are represented in equations (45) to (50) are estimated in each shell whose thickness does not exceed that of a « CELL » having critical thickness τ_{crit}. Note that τ_{crit} is determined by the physical character of the medium. Using these operators we calculate the internal field with the help of the procedure described by Peraiah (1984). The frequency-dependent radiation field thus calculated is transformed on to the observer's frame at infinity.

3. Discussion of the computations.

Our objective is to compute the effects of the presence of dust on the formation of the lines. The number of parameters is quite large and this results in a huge amount of output in the form of line profiles. We have chosen trapezoidal points for frequency integration and Gauss-Legendre points for angle integration. We have employed nine frequency points ($I = 9$) with one frequency point always at the line centre and two angles ($m = 2$) in each half space. Thus the matrix size is (18×18). With this size of frequency-angle mesh, we obtain a stepsize which gives solution to the accuracy permitted by the computer precision. This was done by subjecting the program for the condition of flux conservation in a conservatively scattering medium ($\varepsilon = 0$, $\beta = 0$ and $\omega = 1$). If B and A represent the outer and inner radii of the spherical shell then we always considered a shell with the ratio B/A equal to 3.

The velocity of expansion is assumed to satisfy the equation of continuity, given by

$$4\pi r^2\rho(r)v(r) = \mathrm{Cst}. \tag{51}$$

where $\rho(r)$ and $v(r)$ are the density and velocity of expansion at the radial point r. The velocities are measured in Doppler units. We used the electron density to calculate the optical depth. Equation (51) creates several sets of variations in density ρ and velocity of expansion. We have considered the following sets of variations together with two cases of dust distribution :

$$\tau_d = \text{Cst.} \quad \text{and} \quad \tau_d \sim r\,, \tag{52}$$

$$\rho \sim r^{-2}\,, \quad v = \text{Cst.}\,, \tag{53}$$

and

$$\rho \sim r^{-3}\,, \quad v \sim r\,. \tag{54}$$

The above sets are considered in conjunction with the following set of parameters.

$$\varepsilon = 0 \quad \beta = 0\,, \tag{55}$$

and

$$\varepsilon = 10^{-3} \quad \text{and} \quad \beta = 0\,. \tag{56}$$

Boundary condition. — We assume that no radiation is incident from outside the spherical shell at $r = B$ and $\tau = 0$, while radiation of unit intensity is incident at $r = A$, $\tau = \tau_{\max} = T$, in the case of a purely scattering medium. When there is emission from within the medium, no radiation is made incident at either of the two boundaries. Thus, we have :

$$\left.\begin{aligned} U^-(\tau = T, \mu_j) &= 1 \\ U^+(\tau = 0, \mu_j) &= 0 \end{aligned}\right\}\,, \quad (\varepsilon = 0, \beta = 0)\,, \tag{57}$$

and

$$\left.\begin{aligned} U^-(\tau = T, \mu_j) &= 0 \\ U^+(\tau = 0, \mu_j) &= 0 \end{aligned}\right\}\,, \quad (\varepsilon > 0, \beta > 0)\,. \tag{58}$$

In the case of the boundary condition of the frequency derivative, we have :

$$\frac{\partial U^+}{\partial X}\,(\text{at } X = |X_{\max}|) = 0\,. \tag{59}$$

We have set the velocities at $r = A$ as V_A, and at $r = B$ as V_B which is chosen to be 0(5) 20 Doppler widths. If the spherical shell expands with constant velocity, we have :

$$V_A = V_B\,, \tag{60}$$

and if there are velocity gradients, then we have :

$$V_A = 0 \quad \text{and} \quad V_B > 0\,. \tag{61}$$

We describe the profiles in terms of the fluxes integrated over the whole disc *versus* the normalized frequency. The profiles are described in frequency coordinates because of the fact that we have solved the equation of line transfer in the comoving frame (Eqs. (2) and (3)) in the normalized frequency coordinates. Moreover it is customary to present theoretical line profiles in such coordinates (see Avrett and Hummer, 1965 ; Avrett, 1966 ; Kunasz and Hummer, 1975). For comparison between observed line profiles and those calculated from theory, it is necessary to convert both into the same system of units, usually, the wavelength units. We do not find it necessary to do so here as we are not comparing the profiles with any particular observed line. We define another quantity Q (which is equivalent to Y in Mihalas *et al.*, 1975) given by :

$$Q = \frac{X_Q}{X_{\max}}\,, \quad -1 \leqslant Q \leqslant 1\,. \tag{62}$$

The purpose of this kind of representation is to accommodate all profiles corresponding to different velocities in a single figure. We plotted F_Q/F_C (F_Q and F_C being the integrated fluxes at frequency X_Q and in the continuum, respectively) with respect to Q. The results are presented in the figures for the following parameters :

$\frac{B}{A}$ = The ratio of the outer to inner radii of the spherical shell. We have set $B/A = 3$ in all cases,
ε = the probability per scattering that a photon is lost by collisional de-excitation,
β = the ratio of the absorption coefficient per unit frequency interval in the continuum to that at the line centre,
V_B = the velocity in Doppler units at the point $r = B$ in the spherical medium,
ρ = density of the gas,
V = the velocity of expansion of the shell,
τ_d = total dust optical depth,
T = total gas optical depth at the line centre.

We divided the spherical shell into 30 elementary shells and computed the emergent as well as the internal radiation field by using the algorithm described by Peraiah (1984). The gas optical depths in each shell are calculated according to the density variation shown in the corresponding figure. When the dust optical depth is maintained uniform, say τ_d (total) = 2, then each of the shells will have dust optical depth $\tau_d = 2/30$. However, this will change when τ_d increases with radius.

The profiles are presented in figures 1-80. In figures 1-5, we described the flux profiles for a spherical medium in which the distribution of dust is constant. The total gas optical depth is equal to 45. The density changes as r^{-2}, while the velocity of expansion remains constant satisfying the equation of continuity given in equation (51). This implies that $V = V_A = V_B$ and that there are no velocity gradients. We increased the value of V progressively by 5 Doppler units from $V = 0$ in figure 1 to $V = 20$ in figure 5. In all these figures we have set $\varepsilon = \beta = 0$. Each figure contains 6 profiles corresponding to $\tau_d = 0(1)\,5$. We must remember here that τ_d represents the optical depth due to scattering by dust only. The profiles in figure 1 represent emission from

static medium. We notice that the deepest absorption core is obtained when there is no dust present. As we increase the dust content in the medium the absorption core slowly rises because the dust scatters more photons into the line core formed in a static medium. At $\tau_d = 5$, the line shows least amount of absorption. In figure 2, we introduced a velocity of expansion equal to 5 Doppler units without velocity gradients keeping the other parameters same as those in figure 1. We notice that all lines have a uniform blue shift and that the lines corresponding $\tau_d = 0$ and $\tau_d = 5$ have maximum and minimum absorptions, respectively.

In figure 3, we increased the velocity of expansion V to 10 Doppler units. Although all the profiles show blue shift, the absorption characteristics do not show a monotonic behaviour as shown in figures 1 and 2. The absorption core of the dust free profile is intermediate between the profiles corresponding to $\tau_d = 1$ and $\tau_d = 5$ which have maximum and minimum amounts of absorption, respectively, in their cores. Profiles for $V = 15$ Doppler units show a behaviour similar to those of figure 3. When V is increased to 20, the profiles become very narrow and the amount of absorption in the cores of the lines formed in the presence of dust do not show any monotonic behaviour. In figures 6-10, we have presented profiles emerging out of the medium in which the velocity varies linearly with the radius. This introduces velocity gradients and the amount of dust is kept constant as in the case of the profiles shown in figures 1-5. Dust affects the profiles in a different way unlike the case of figure 1, the dust free profile shows minimum absorption and the profile for $\tau_d = 1$ shows maximum absorption. For $\tau_d > 1$, the dust begins to scatter more and more photons into the line core, while the profiles for $0 < \tau_d < 1$ indicate that the dust removes photons from the core of the line. When $V_A = 0$ and $V_B = 5$ (see Fig. 7) the profiles are blue-shifted and the amount of absorption corresponding to each τ_d is non-monotonic. The profiles in figures 8-10 show characteristics similar to those in figure 7. We changed the mode of variation of the dust component in that τ_d and the expansion velocity each is allowed to increase outward with radius and the gas density is allowed to vary as r^{-3}. The resulting profiles are displayed in figures 11-15. We notice that there is slight emission in the wings in the case of static medium. The dust free profile has minimum absorption core while the profile corresponding to maximum amount of dust has deepest absorption core (e.g. $\tau_d = 5$). It may be noted that the core absorption increases monotonically with the amount of dust. When the outer velocity V_B in increased to 5, the symmetric profile in figure 11 is rendered asymmetric as shown in figure 12 with red emission and blue absorption similar to P Cygni type of profiles. Now the monotonic behaviour of the absorption core with τ_d is disturbed, although the profiles corresponding to $\tau_d > 3$ have more photons removed from the core by dust. The profiles corresponding to $0 < \tau_d < 2$ show the fact that dust scatters more photons into the line core when the medium is expanding. As the velocity of expansion increases, dust scatters more photons into the line core as revealed by the profiles given in figures 13-15 ; while the characteristics of the P Cygni type profile have been maintained. In figures 16-20, we kept the density of the gas component varying as r^{-2} and therefore the spherical shell is assumed to expand with a constant velocity. Simultaneously the dust optical depth is taken to vary as r. The profiles given in figure 16 corresponding to a static medium show a monotonic behaviour. However, when expansion is introduced, this trend is changed as shown in figures 17-20.

In figures 21-40, we have presented profiles corresponding to $\varepsilon = 10^3$ and $\beta = 0$. We can see that all those profiles formed in static media show emission profiles with central absorption. When the dust with optical depth in the range of $0 < \tau_d < 1$ is introduced, the emission is drastically reduced. A further increase in τ_d such that $\tau_d > 2$, the line totally disappears with rapid expansion. When expansion is introduced, instead of two symmetric peaks of emission we obtain a single peak of emission. The presence of dust reduces the emission and in few cases a small amount of blue absorption is produced. In figures 41-80, we present profiles for $\tau_{\text{gas}} = 445$ and 300 but in media whose physical characteristics are similar to those studied in figures 1-40. Once again these profiles show similar characteristics.

4. Conclusions.

We computed line profiles formed in a dusty and expanding spherical medium. We have considered dust scattering optical depth as high as 5 but no absorption due to dust is included. In a static medium, the profiles show a monotonic behaviour with increasing dust optical depth. However, in a expanding medium, dust changes the profiles in a different manner, in several cases the profiles change variously in a non-monotonic manner.

Acknowledgements.

One of us (A. P.) would like to thank the members of the Institut für Theoretische Astrophysik, Heidelberg, for their hospitality during his brief stay there. He wants to thank Dr. R. Wehrse in particular, for his kindness and allowing him to use part of his computer time and for several fruitful discussions on the effects of dust. We also like to express gratefully our thanks to Dr. P. Kunasz for his useful comments which improved the quality of the paper.

References

ALLEN, D. A. : 1973, *Mon. Not. R. Astron. Soc.* **161,** 145.
ALLEN, D. A., SWINGS, J. P. : 1972, *Astrophys. Lett.* **10,** 83.
AVRETT, E. : 1966, *Astrophys. J.* **144,** 59.
AVRETT, E., HUMMER, D. : 1965, *Mon. Not. R. Astron. Soc.* **130,** 295.
CHANDRASEKHAR, S. : 1945, *Rev. Mod. Phys.* **17,** 138.
FELLI, M. : 1982, *Mem. Soc. Acad. It.* **53,** 349.
GRASDALEN, G. L. : 1976, *Astrophys. J. Lett.* **205,** L83.
GEISEL, S. L. : 1970, *Astrophys. J. Lett.* **161,** L105.
HUGGINS, P. J., GLASSGOLD, MORRIS, M. : 1984, *Astrophys. J.* **279,** 284.
HENKEL, C., MATTHEWS, H. E., MORRIS, M. : 1983, *Astrophys. J.* **267,** 184.
HUMMER, D. G., KUNASZ, P. B. : 1980, *Astrophys. J.* **236,** 609.
KUNASZ, P., HUMMER, D. G. : 1974, *Mon. Not. R. Astron. Soc.* **166,** 19.
KUNASZ, P., HUMMER, D. G. : 1974, *Mon. Not. R. Astron. Soc.* **166,** 57.
KWAN, J., HILLI, F. : 1977, *Astrophys. J.* **215,** 781.
MIHALAS, D. : 1978, *Stellar Atmospheres*, II. ed. (Freeman, San Francisco).
MIHALAS, D., KUNASZ, P. B., HUMMER, D. G. : 1975, *Astrophys. J.* **202,** 465.
PERAIAH, A. : 1984, in *Methods in Radiative Transfer*, W. Kalkofen (Ed.) (Cambridge) p. 281.
PERAIAH, A., WEHRSE, R. : 1978, *Astron. Astrophys.* **70,** 213.
PERSI, P., FERRARI-TONILOLO, M., GRASDALEN, G. L. : 1983, *Astrophys. J.* **269,** 265.
SIMON, M., FELLI, M., CASSAR, L., FISCHER, J., MASSI, M. : 1983, *Astrophys. J.* **266,** 623.
SIMON, M., RIGHINI-COHEN, G., FELLI, M., FISCHER, J. : 1981, *Astrophys. J.* **244,** 552.
SCHWARTZ, P. R., THRONSON, J. R., H. A., LADA, C. J., SMITH, H. A., GLACCUM, W., HARPER, D. A., KNOWLES, S. H. : 1983, *Astrophys. J.* **271,** 625.
WEHRSE, R., KALKOFEN, W. : 1985, *Astron. Astrophys.* **147,** 71.
WEHRSE, R., PERAIAH, A. : 1979, *Astron. Astrophys.* **71,** 289.

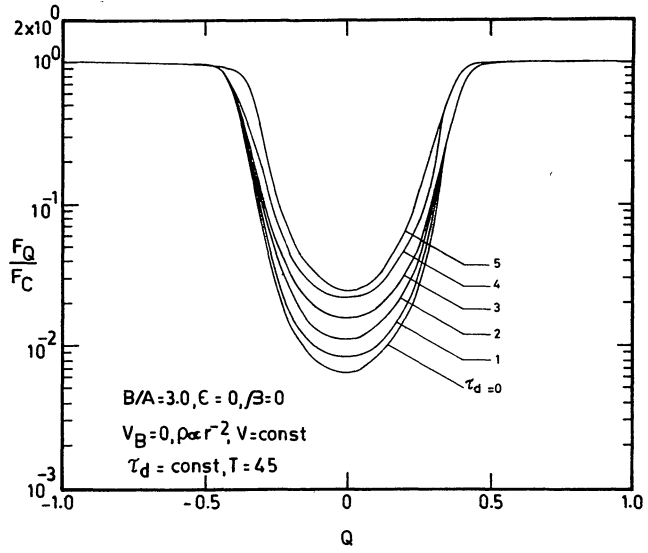

FIGURE 1. — Line profiles formed in a static medium with dust.

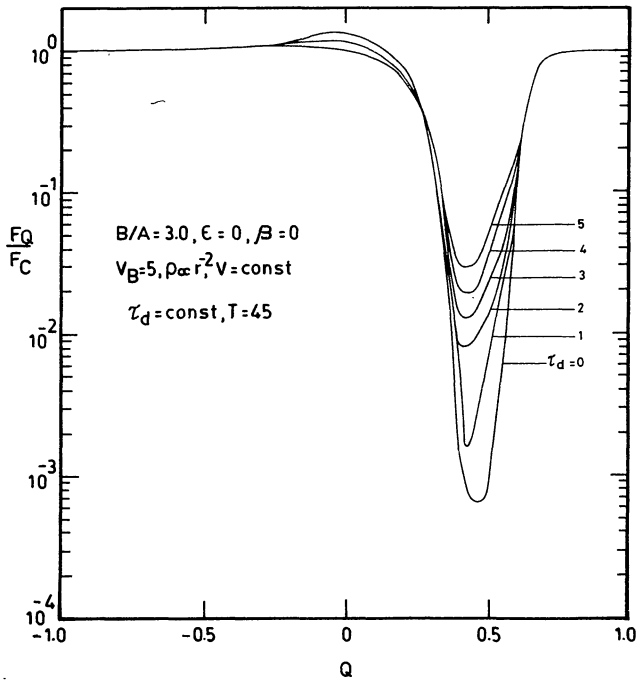

FIGURE 2. — Line profiles formed in a medium moving with a constant velocity of 5 Doppler units (no velocity gradients), with dust.

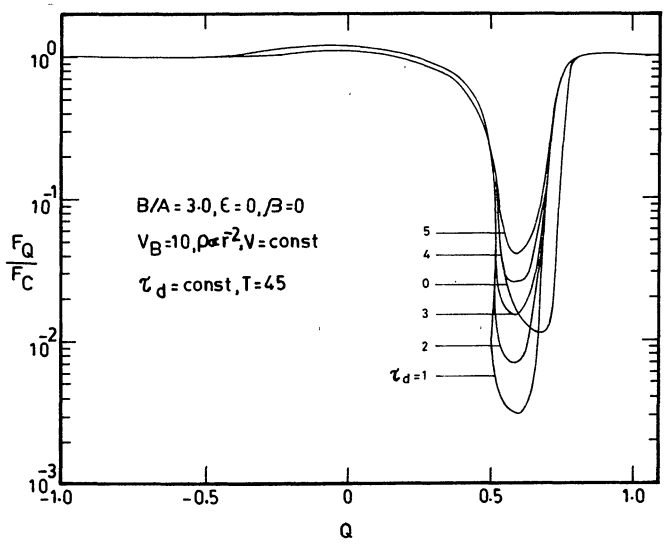

FIGURE 3. — Same as those given in figure 2 but with velocity of expansion equal to 10 Doppler units.

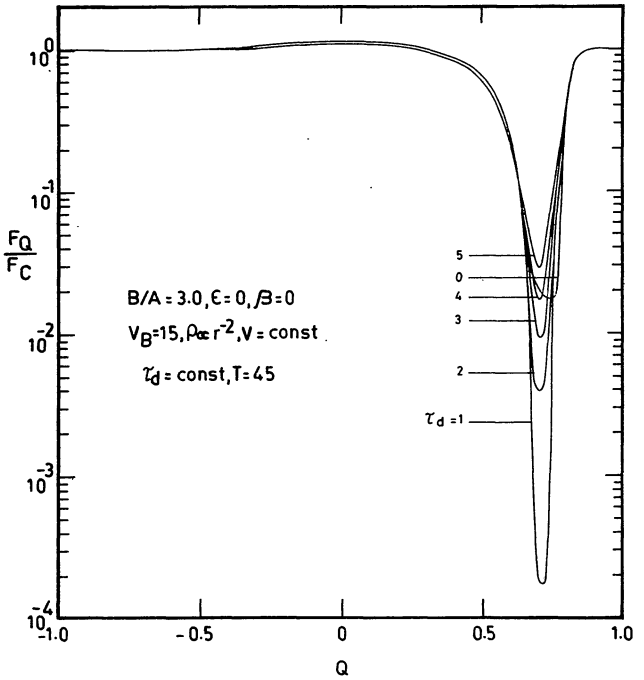

FIGURE 4. — Same as those given in figure 2 but with velocity of expansion equal to 15 Doppler units.

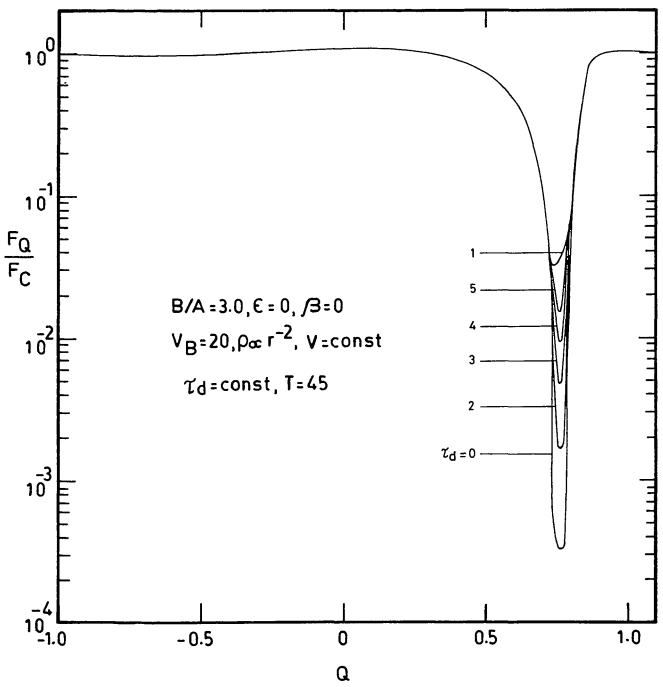

FIGURE 5. — Same as those given in figure 2 but with velocity of expansion equal to 20 Doppler units.

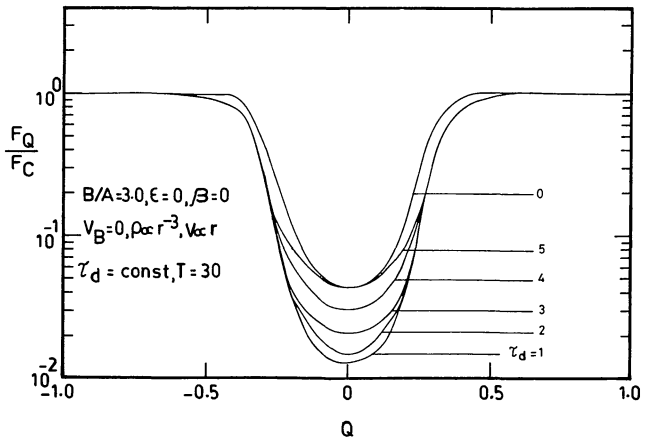

FIGURE 6. — Line profiles in a static medium in which the gas density varies as r^{-3} and with constant distribution of the dust.

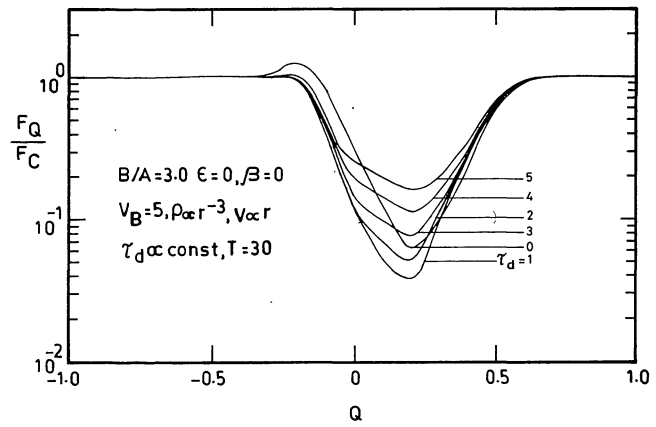

FIGURE 7. — Same as those given in figure 6 with velocity gradients and the velocity of expansion $V_B = 5$ Doppler units.

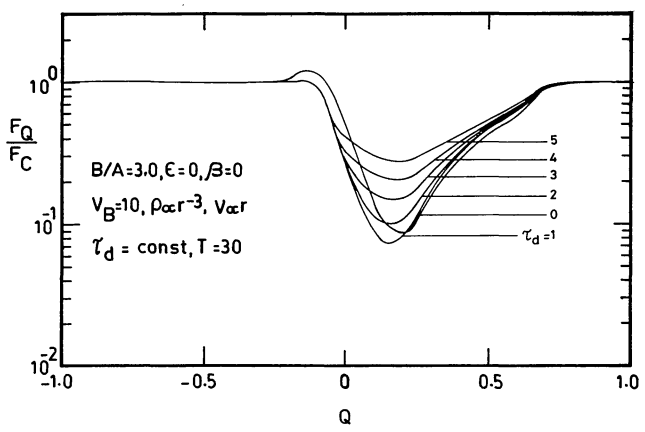

FIGURE 8. — Same as those given in figure 7 but with velocity of expansion $V_B = 10$ Doppler units.

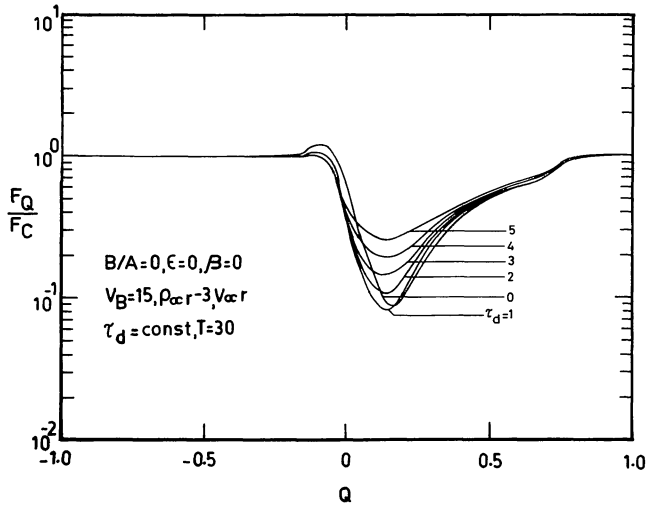

FIGURE 9. — Same as those given in figure 7 but with velocity of expansion $V_B = 15$ Doppler units.

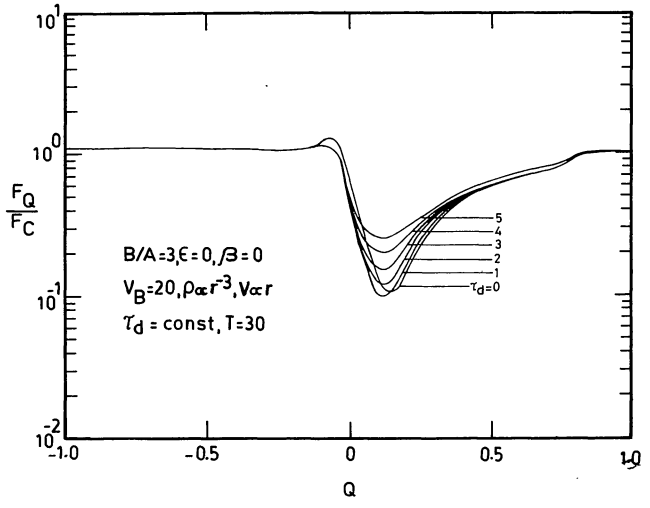

FIGURE 10. — Same as those given in figure 7 but with the velocity of expansion $V_B = 20$ Doppler units.

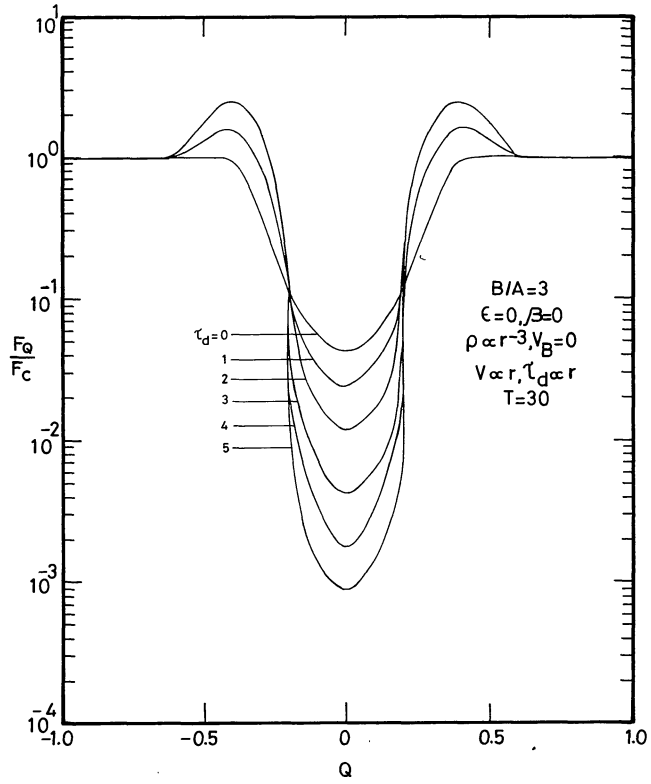

FIGURE 11. — Line profiles formed in a static medium with dust changing proportionately with r and the gas density changing as r^{-3}.

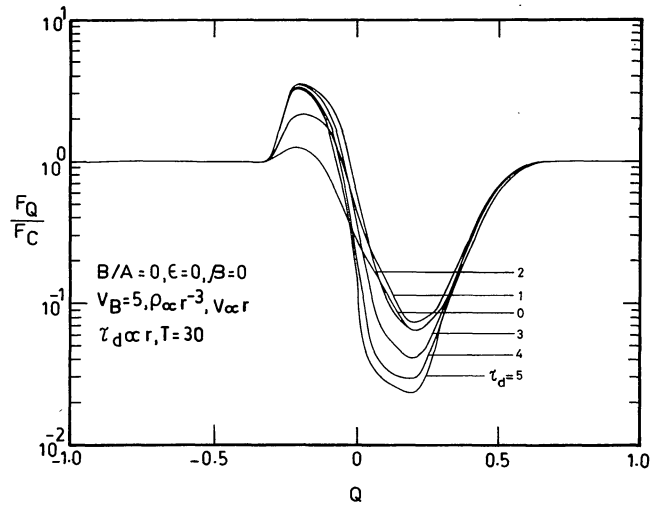

FIGURE 12. — Same as those given in figure 11 but with the velocity of expansion $V_B = 5$ Doppler units.

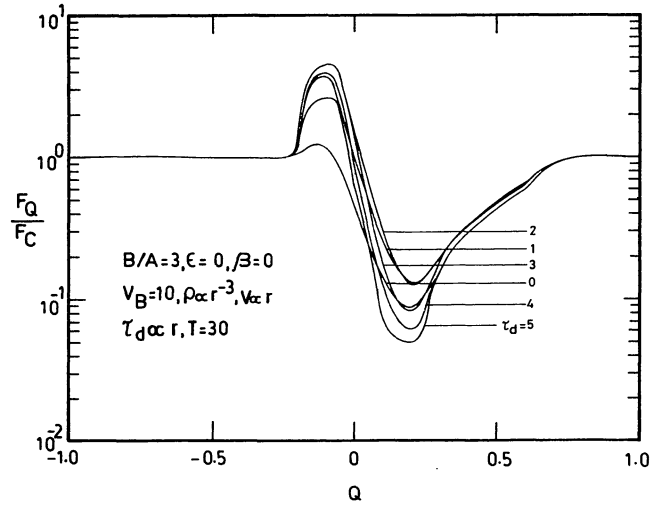

FIGURE 13. — Same as those given in figure 12 with $V_B = 10$ Doppler units.

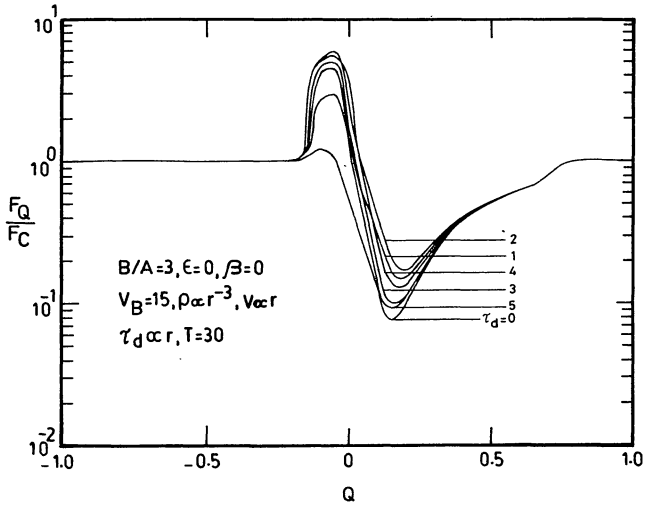

FIGURE 14. — Same as those given in figure 12 but with $V_B = 15$ Doppler units.

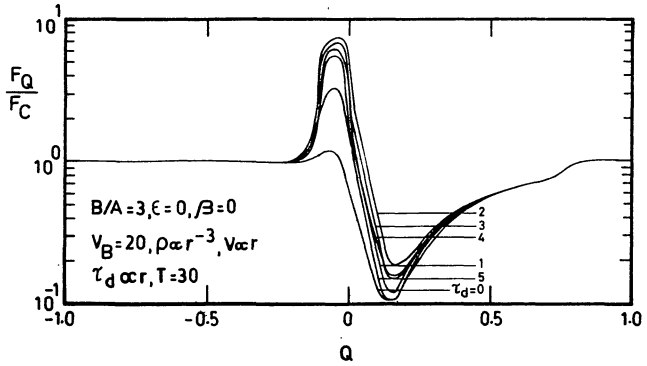

FIGURE 15. — Same as those given in figure 12 but with $V_B = 20$ Doppler units.

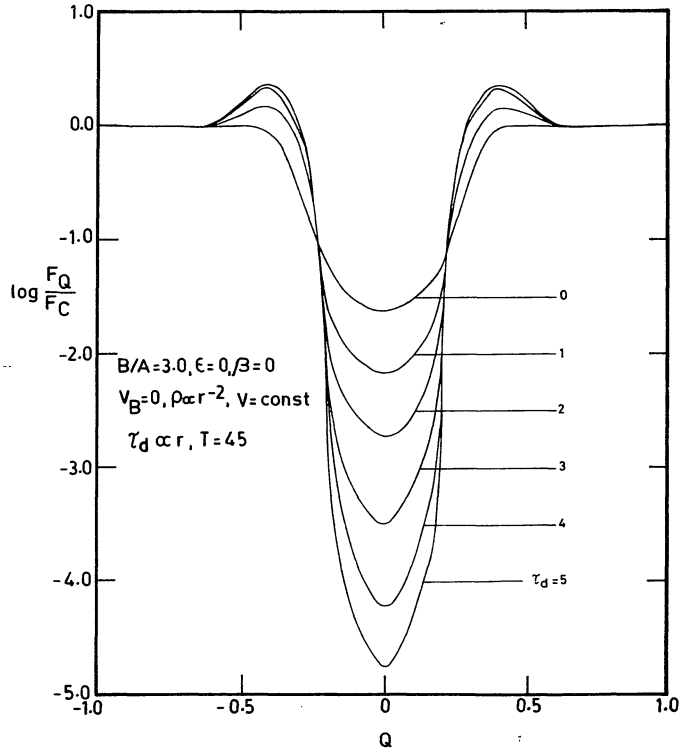

FIGURE 16. — Line profile formed in static medium in which dust changes proportionately with r and the gas density changes as r^{-2}.

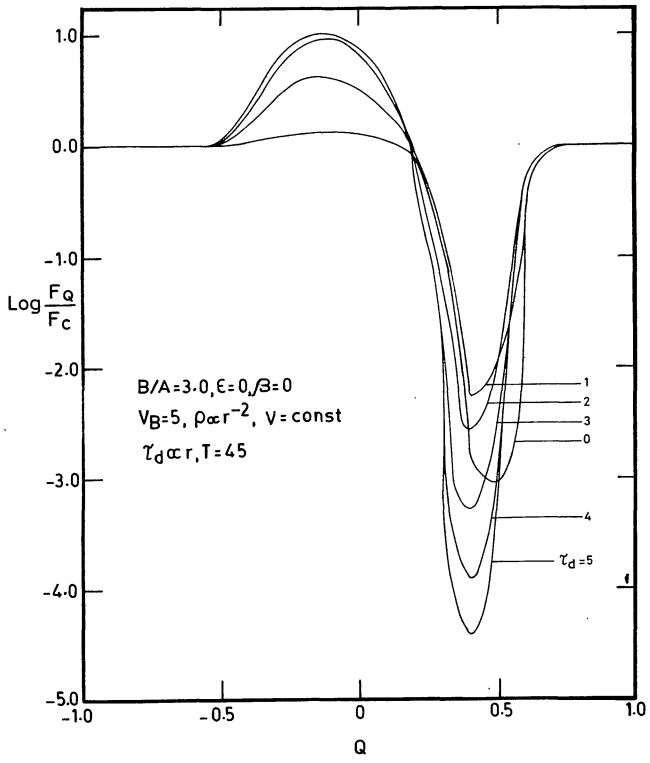

FIGURE 17. — Same as those given in figure 16 with no velocity gradients but the medium is expanding with 5 Doppler units ($V_B = 5$).

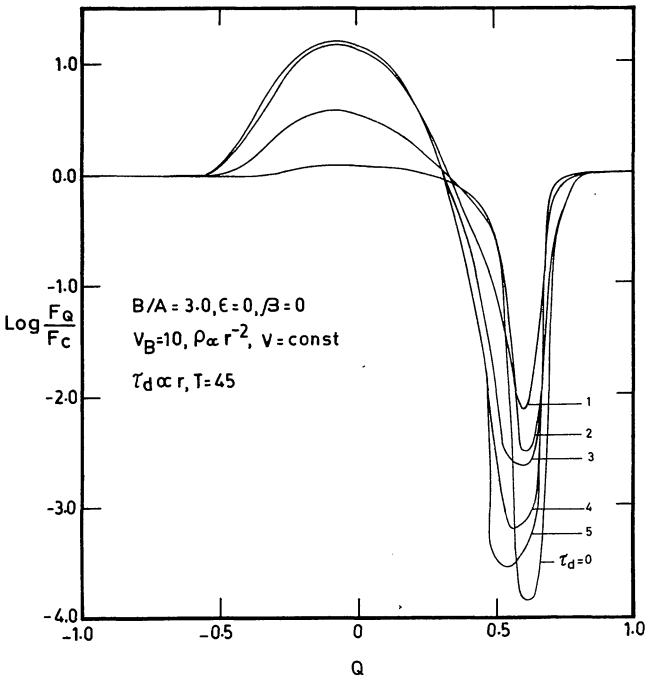

FIGURE 18. — Same as those given in figure 17 but with $V_B = 10$ Doppler units.

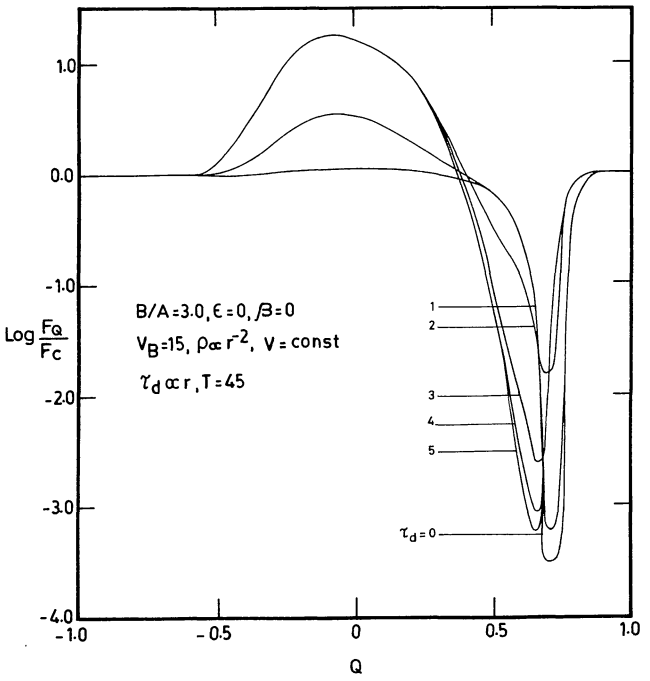

FIGURE 19. — Same as those given in figure 17 but with $V_B = 15$ Doppler units.

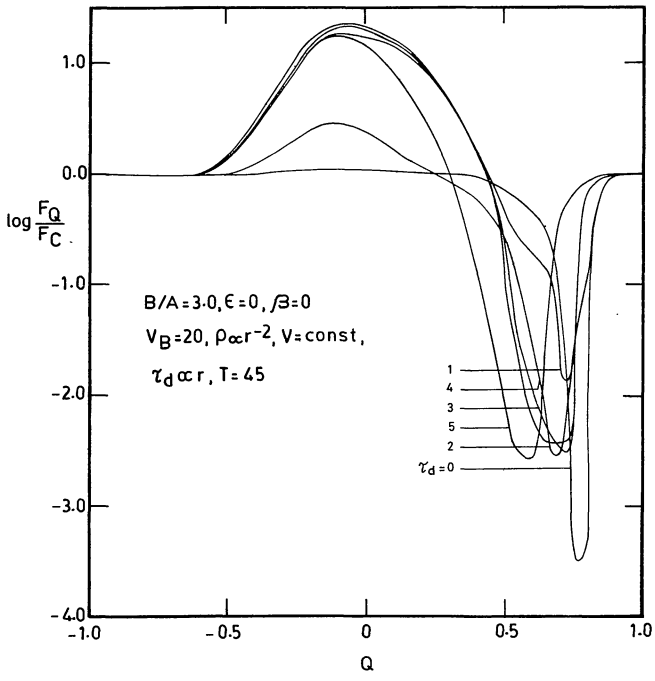

FIGURE 20. — Same as those given in figure 17 but with $V_B = 20$ Doppler units.

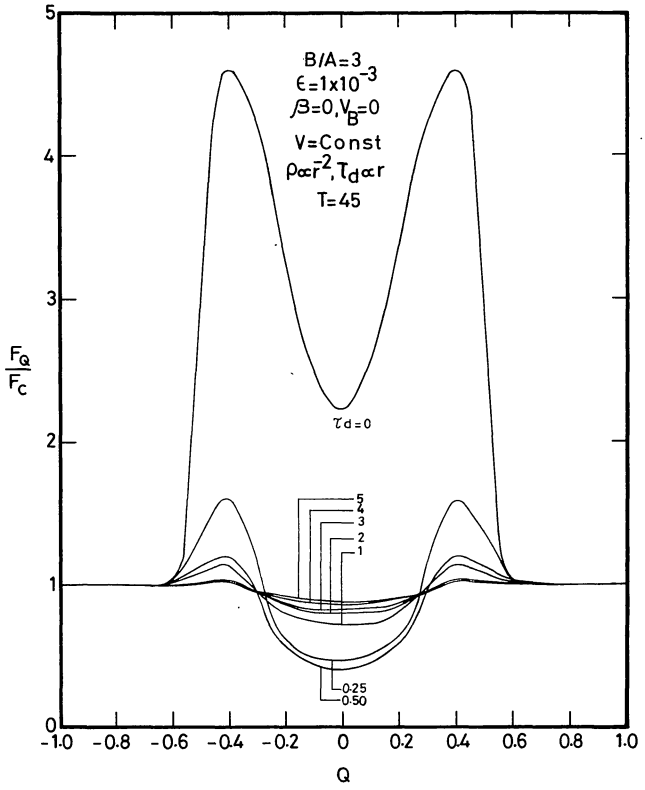

FIGURE 21. — Line profiles formed in a static medium in which there is line emission and the dust is changing proportionately with r and gas density is changing as r^{-2}.

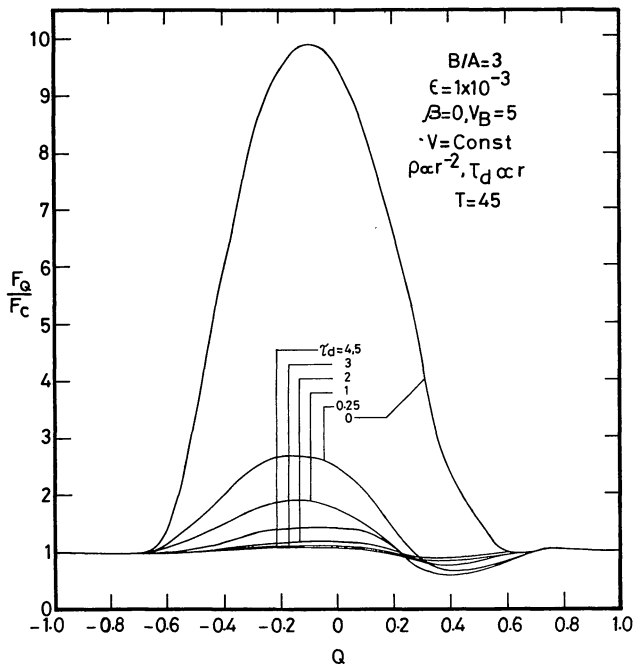

FIGURE 22. — Same as those given in figure 21 but the medium is expanding with velocity of 5 Doppler units and no velocity gradients.

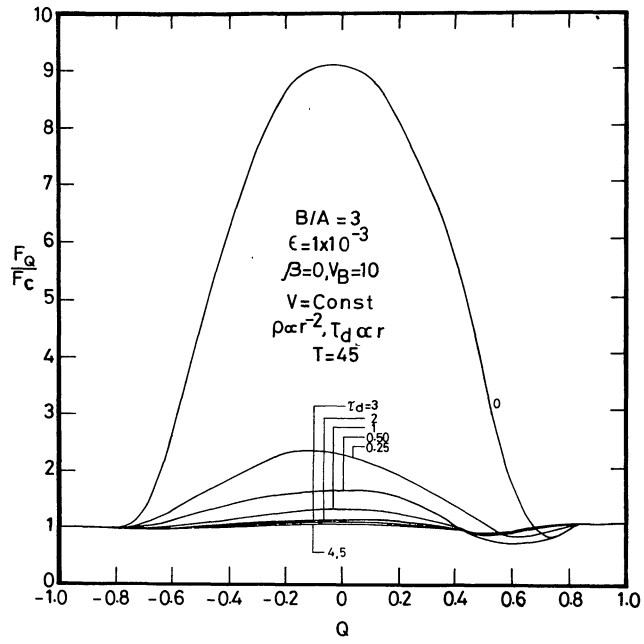

FIGURE 23. — Same as those given in figure 22 but with velocity of expansion $V_B = 10$ Doppler units.

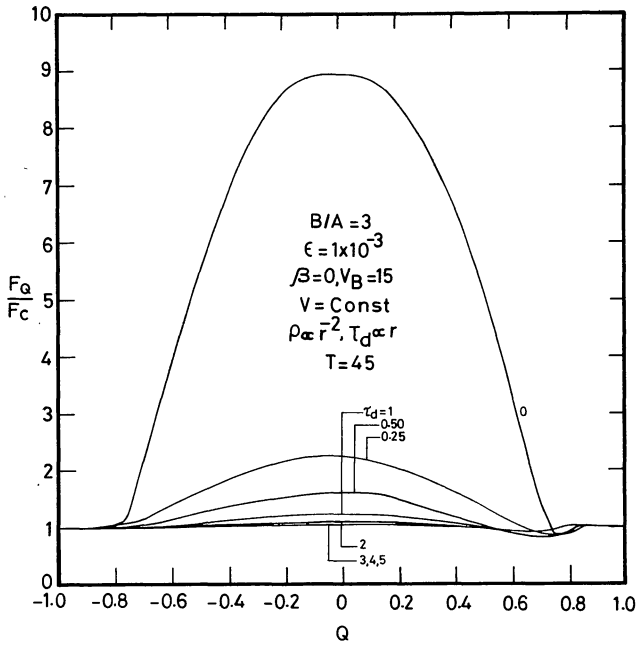

FIGURE 24. — Same as those given in figure 22 but with the expanding velocity $V_B = 20$ Doppler units.

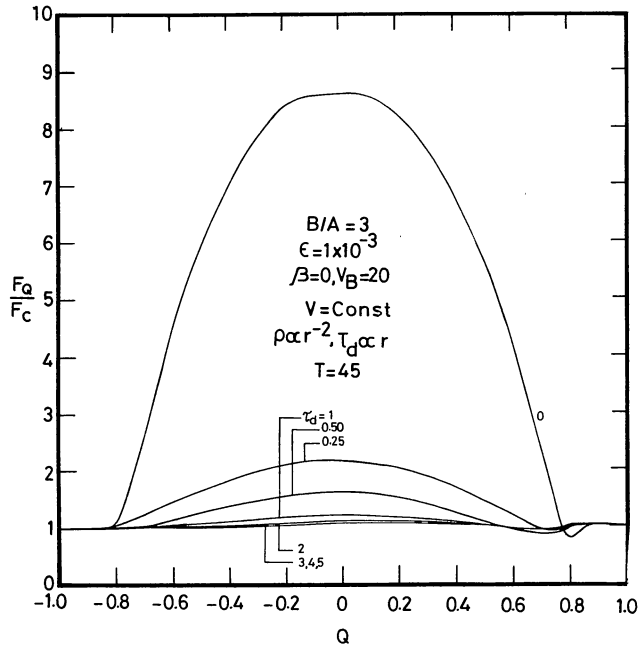

FIGURE 25. — Same as those given in figure 22 but with expanding velocity $V_B = 20$ Doppler units.

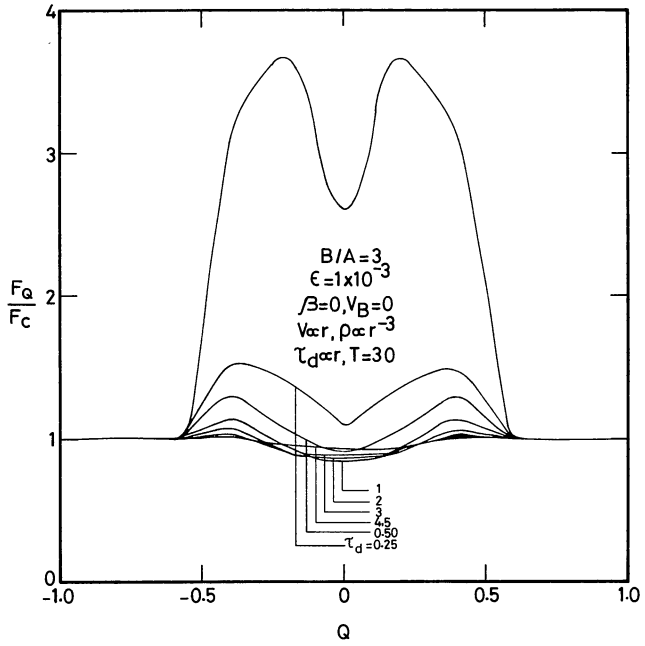

FIGURE 26. — Line profiles formed in a static medium with line emission and the dust optical depth is increasing with the radius while gas optical depth changes as r^{-3}.

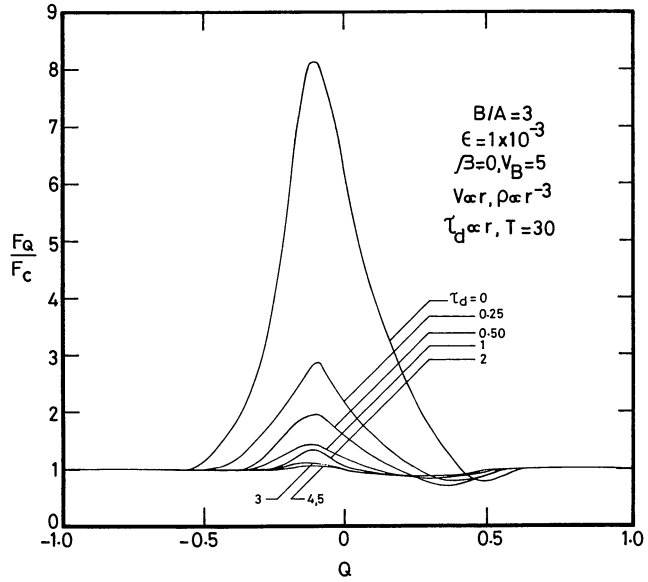

FIGURE 27. — Same as those given in figure 26 but with velocity gradients and $V_B = 5$ Doppler units.

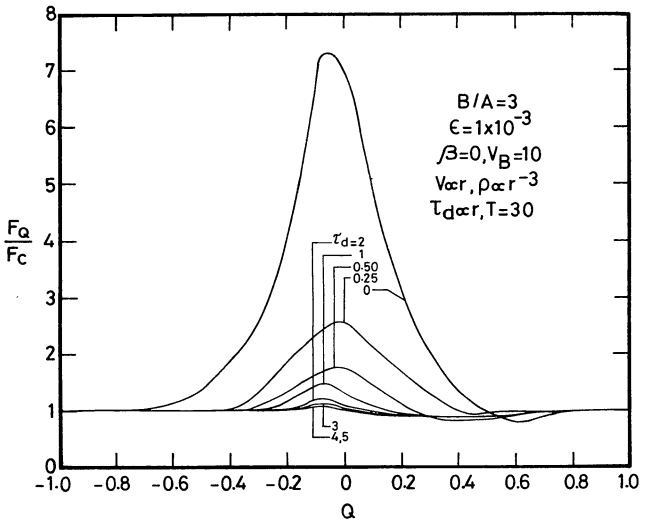

FIGURE 28. — Same as those given in figure 27 but with $V_B = 10$ Doppler units.

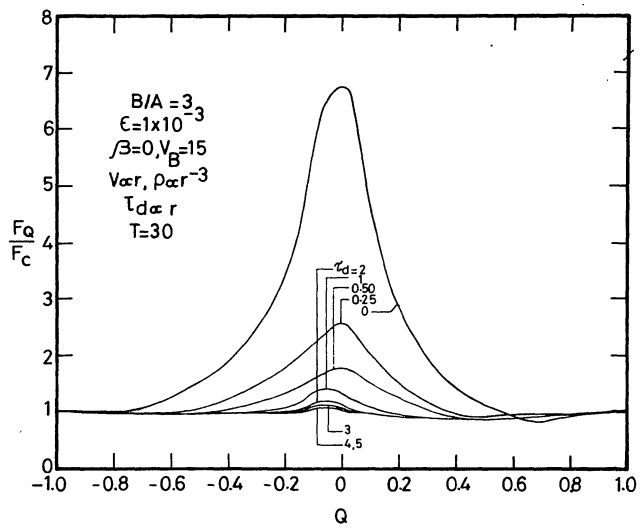

FIGURE 29. — Same as those given in figure 27 but with $V_B = 15$ Doppler units.

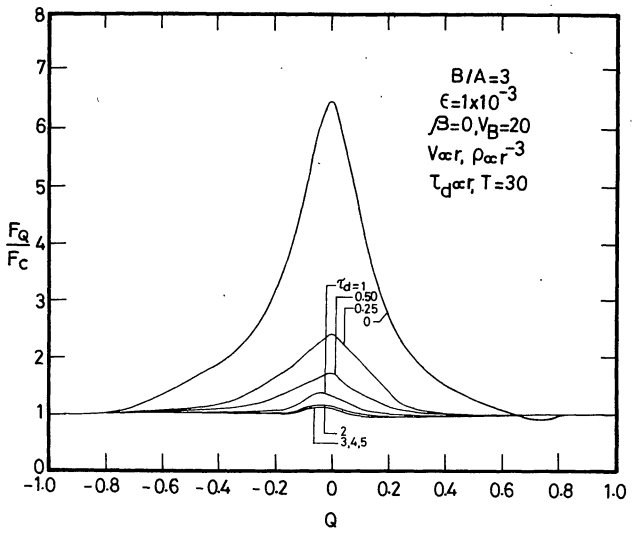

FIGURE 30. — Same as those given in figure 27 but with $V_B = 20$ Doppler units.

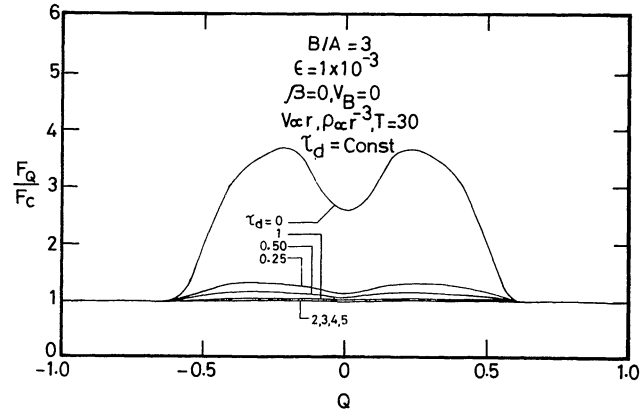

FIGURE 31. — Line profiles formed in a static medium in which there is line emission. The dust is distributed uniformly and the gas density changes as r^{-3}.

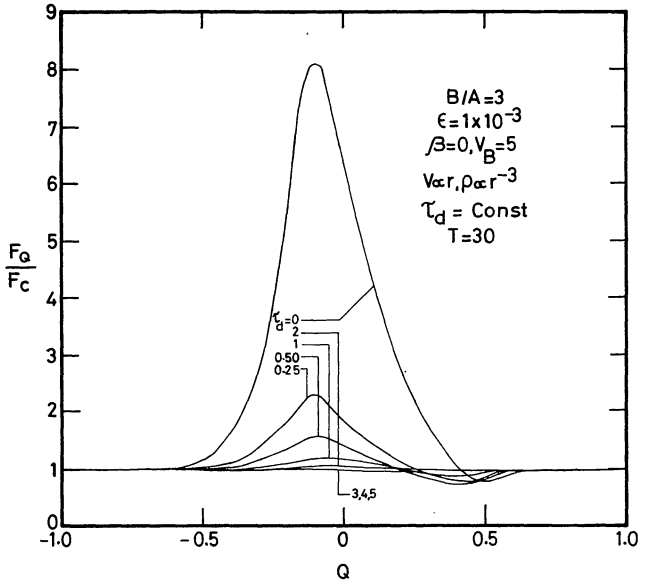

FIGURE 32. — Same as those given in figure 31 but with velocity gradients and $V_B = 5$ Doppler units.

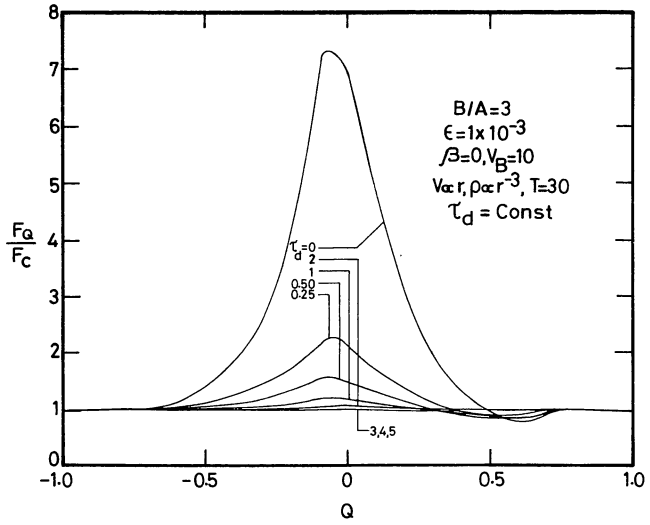

FIGURE 33. — Same as those given in figure 32 but with $V_B = 10$ Doppler units.

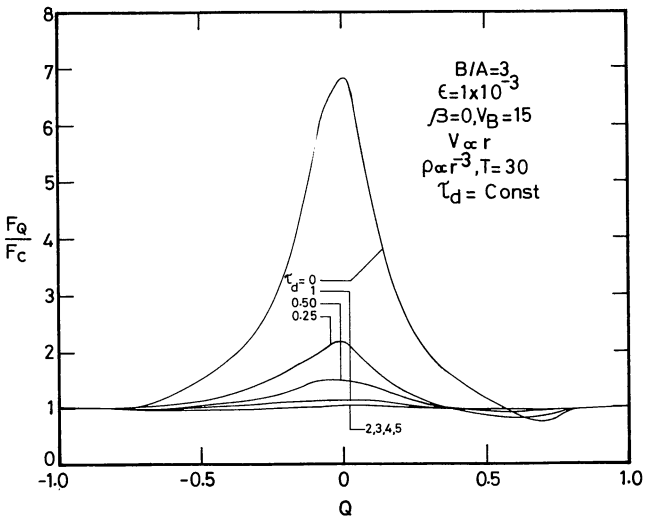

FIGURE 34. — Same as those given in figure 32 but with $V_B = 15$ Doppler units.

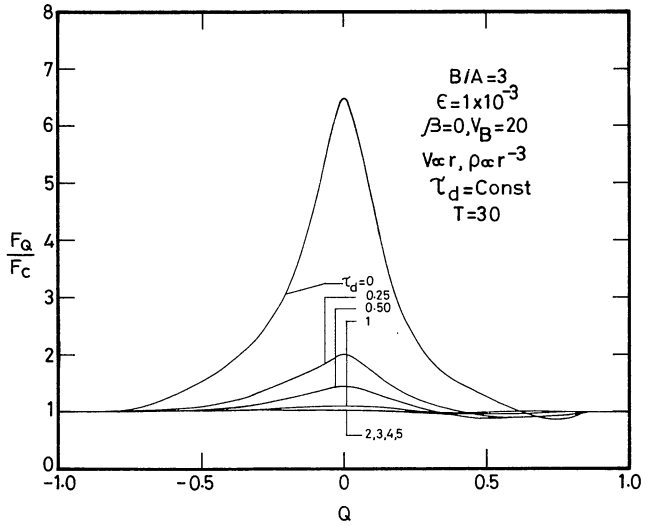

FIGURE 35. — Same as those given in figure 32 but with $V_B = 20$ Doppler units.

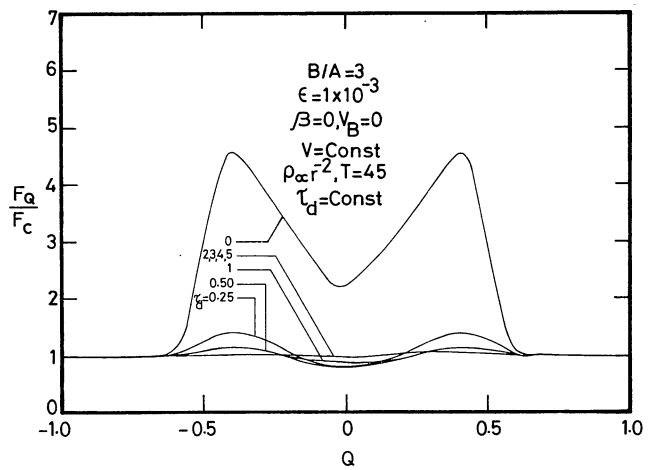

FIGURE 36. — Line profiles formed in a static medium in which dust is distributed uniformly and the gas density changes as r^{-2} with line emission.

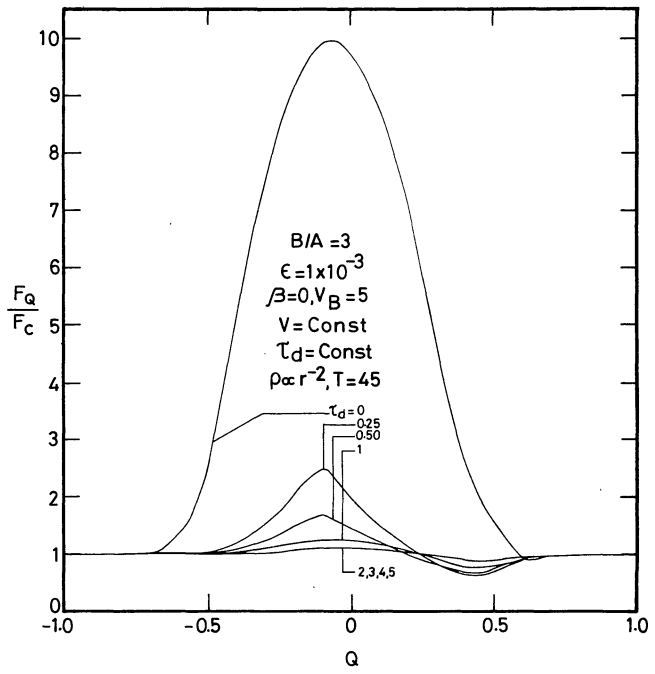

FIGURE 37. — Same as those given in figure 36 but with an expansion velocity for $V_B = 5$ Doppler units without velocity gradients.

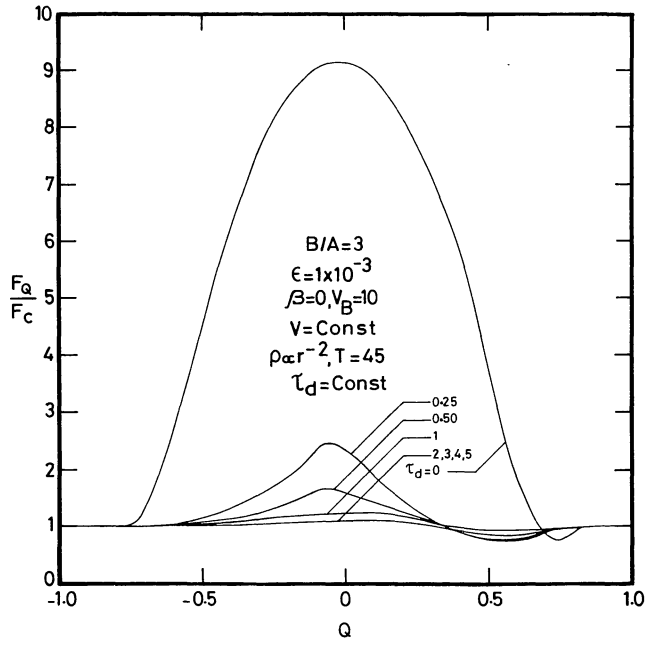

FIGURE 38. — Same as those given in figure 37 but with $V_B = 10$ Doppler units.

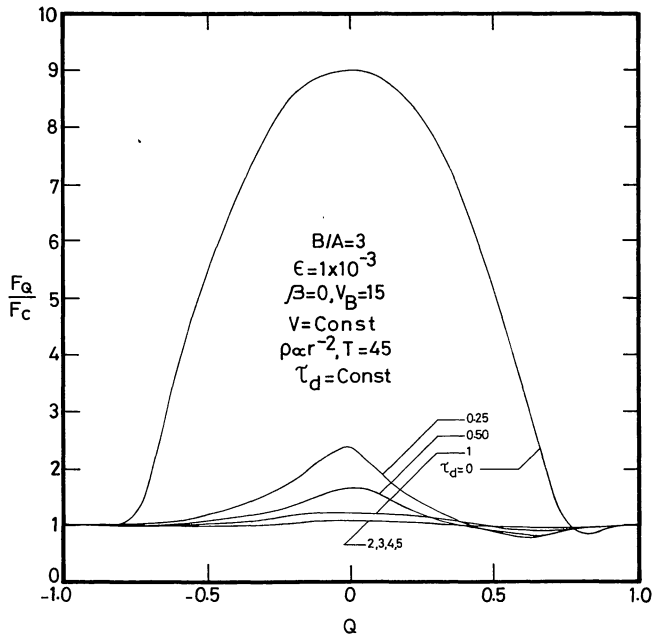

FIGURE 39. — Same as those given in figure 37 but with $V_B = 15$ Doppler units.

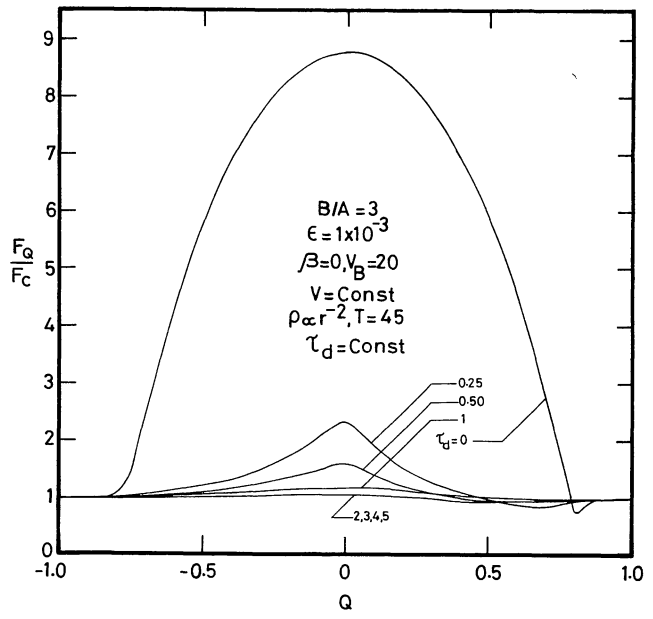

FIGURE 40. — Same as those given in figure 37 but with $V_B = 20$ Doppler units.

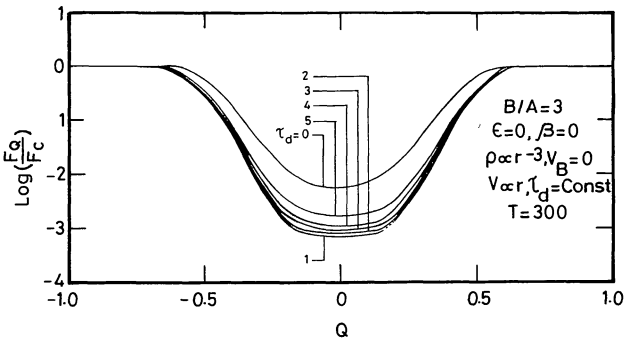

FIGURE 41. — Line profiles formed in static medium with constant dust distribution and with gas density changing as r^{-3}. The total optical depth $T = 300$.

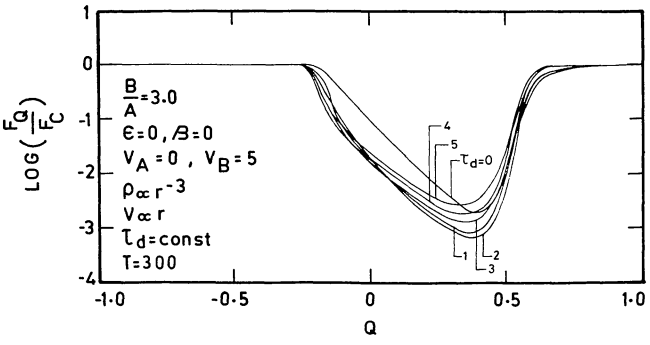

FIGURE 42. — Same as those given in figure 41 but formed in a medium expanding with velocity gradients ($V_B = 5$ Doppler units).

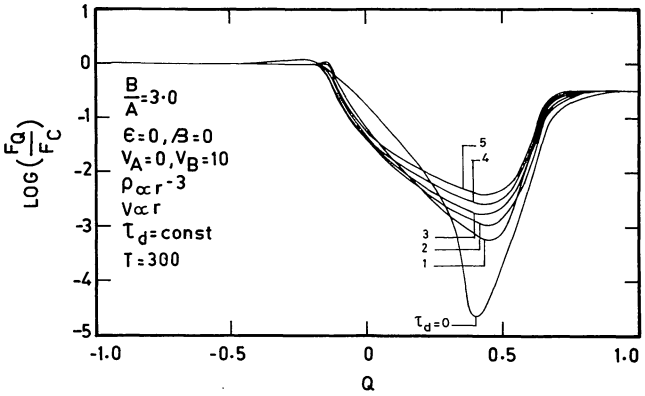

FIGURE 43. — Same as those given in figure 42 but with $V_B = 10$ Doppler units.

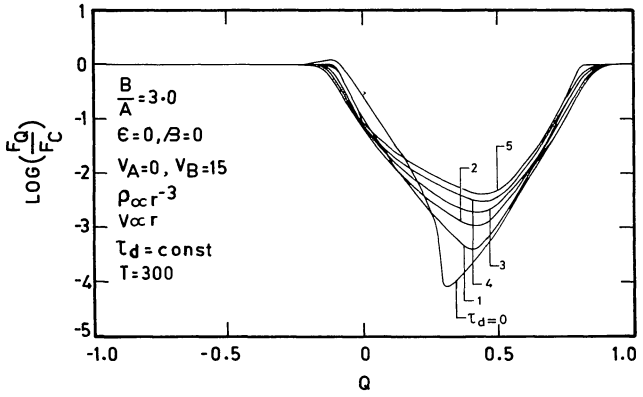

FIGURE 44. — Same as those given in figure 42 but with $V_B = 15$ Doppler units.

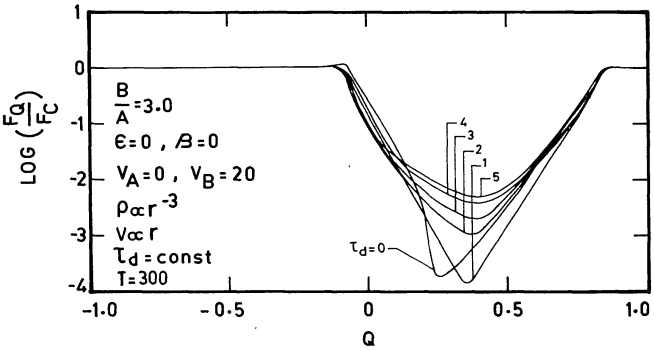

FIGURE 45. — Same as those given in figure 42 but with $V_B = 20$ Doppler units.

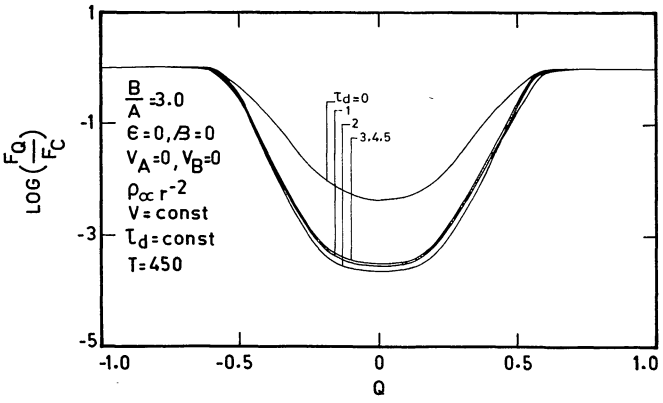

FIGURE 46. — Line profiles formed in static medium with uniform distribution of dust and with total gas optical depth $T = 450$.

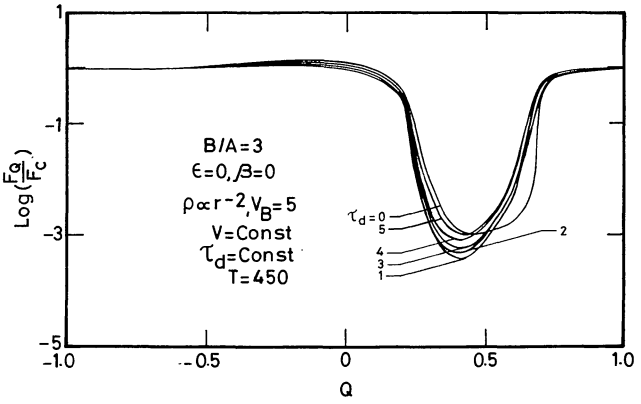

FIGURE 47. — Same as those given in figure 46 but with $V_B = 5$ Doppler units without velocity gradients.

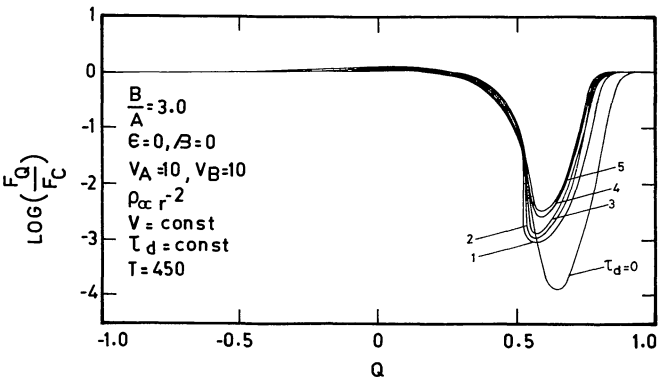

FIGURE 48. — Same as those given in figure 47 but with $V_B = 10$ Doppler units.

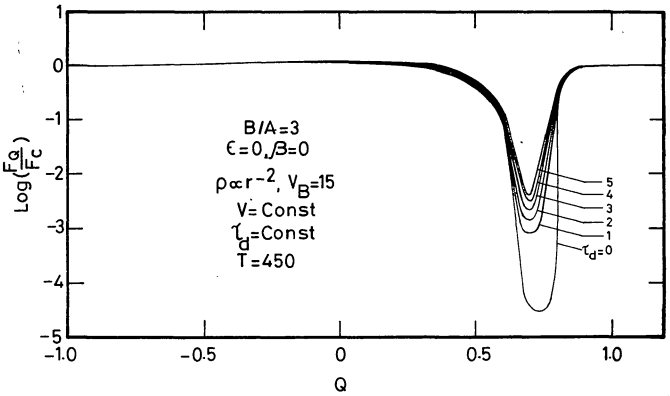

FIGURE 49. — Same as those given in figure 47 but with $V_B = 15$ Doppler units.

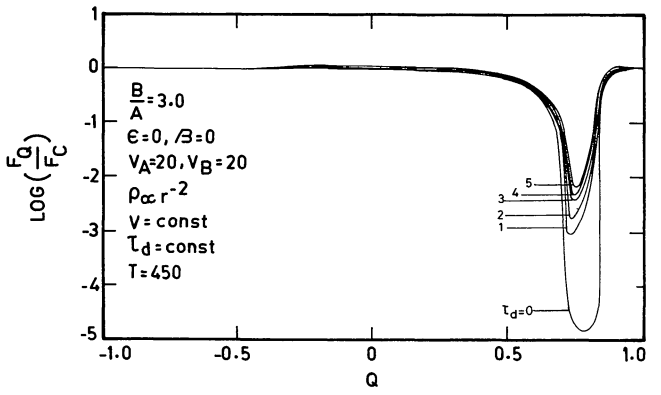

FIGURE 50. — Same as those given in figure 47 with $V_B = 20$ Doppler units.

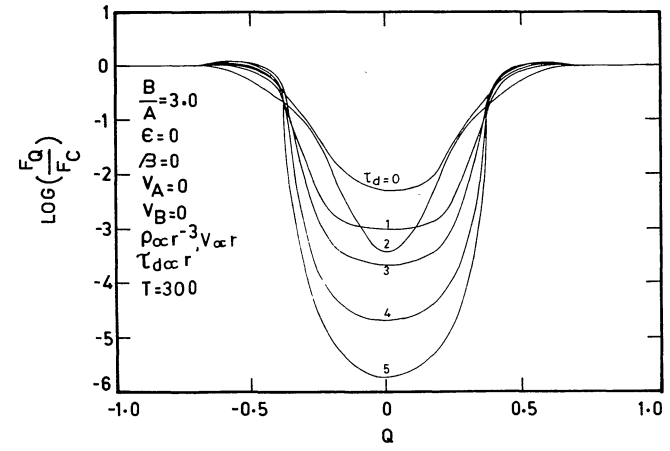

FIGURE 51. — Line profiles formed a static medium with uniform dust distribution and with gas density changing as r^{-3}. Total gas optical depth $T = 300$.

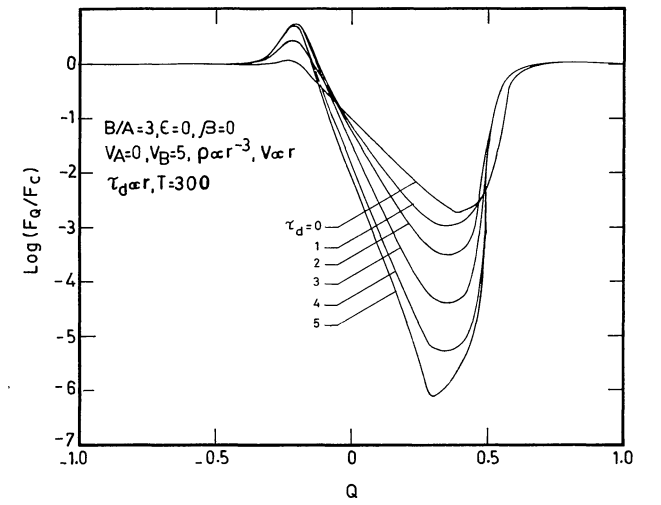

FIGURE 52. — Same as those given in figure 51 but with $V_B = 5$ Doppler units and the medium is moving with velocity gradients.

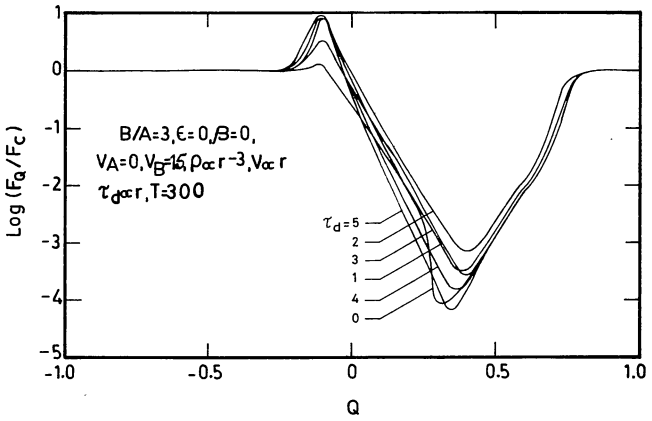

FIGURE 53. — Same as those given in figure 52 but with $V_B = 10$ Doppler units.

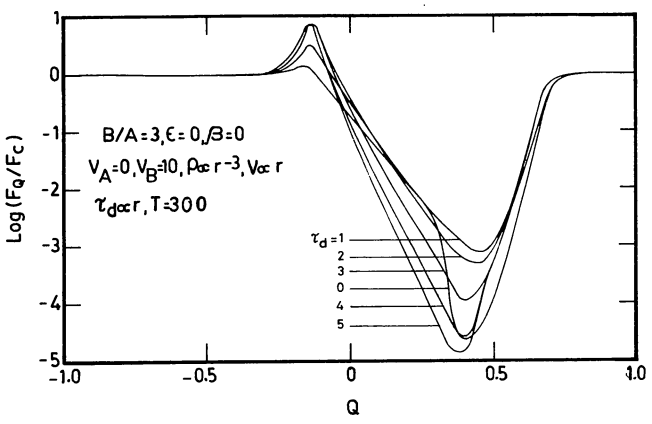

FIGURE 54. — Same as those given in figure 52 but with $V_B = 15$ Doppler units.

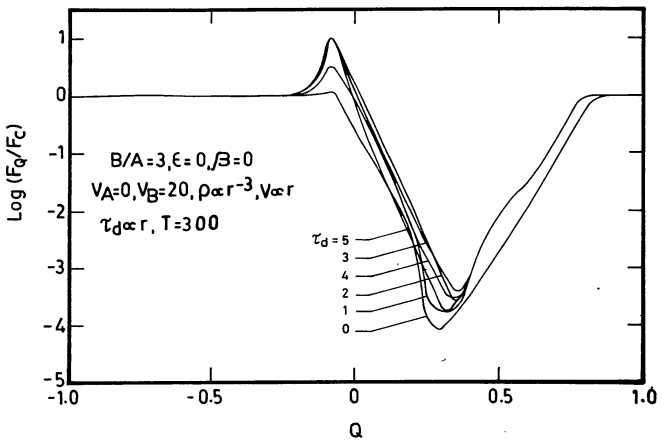

FIGURE 55. — Same as those given in figure 52 but with $V_B = 20$ Doppler units.

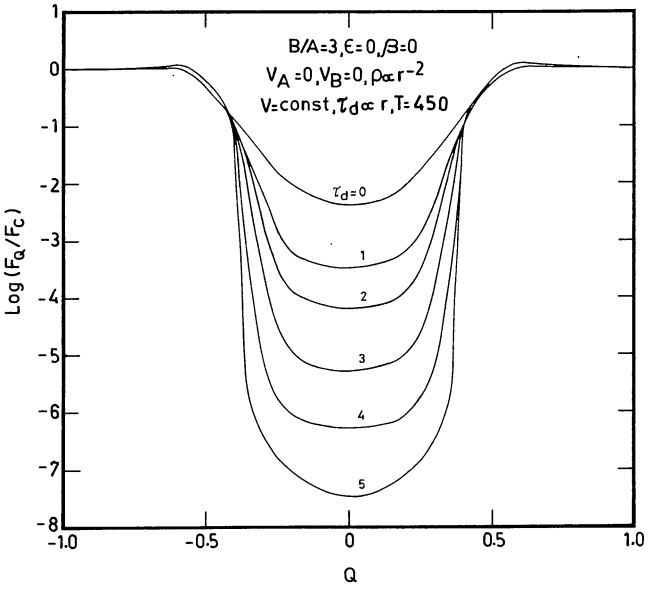

FIGURE 56. — Line profiles formed in a static medium in which dust density increases proportionately with r and the gas density changes as r^{-2}. The total gas optical depth $T = 450$.

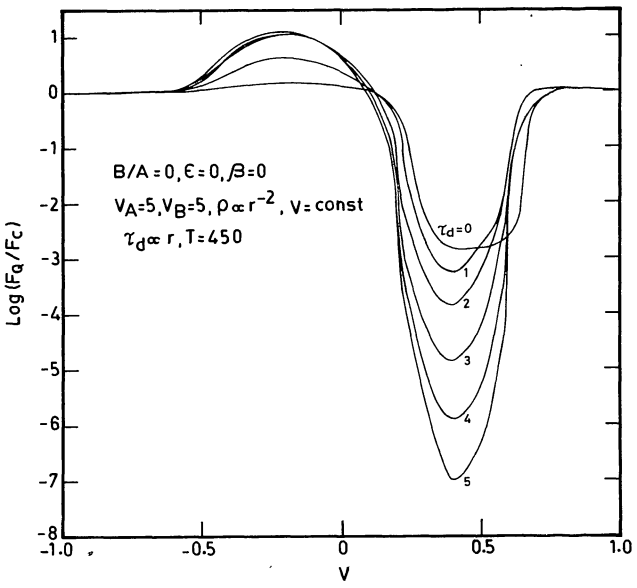

FIGURE 57. — Same as those given in figure 56 but with expansion velocity V_B = 5 Doppler units without velocity gradients.

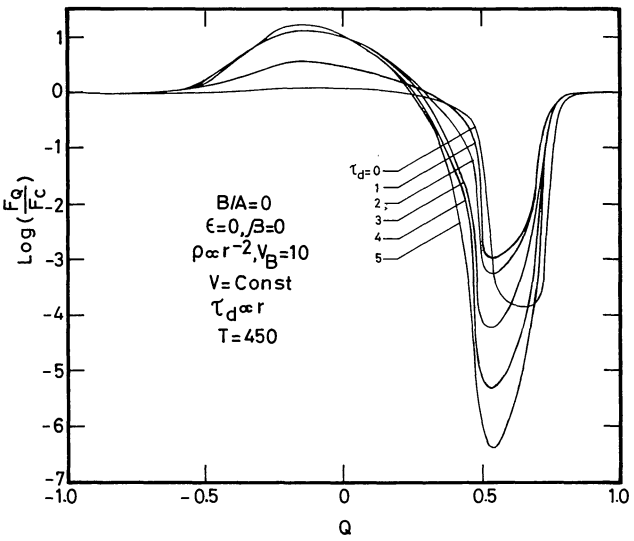

FIGURE 58. — Same as those given in figure 57 but V_B = 10 Doppler units.

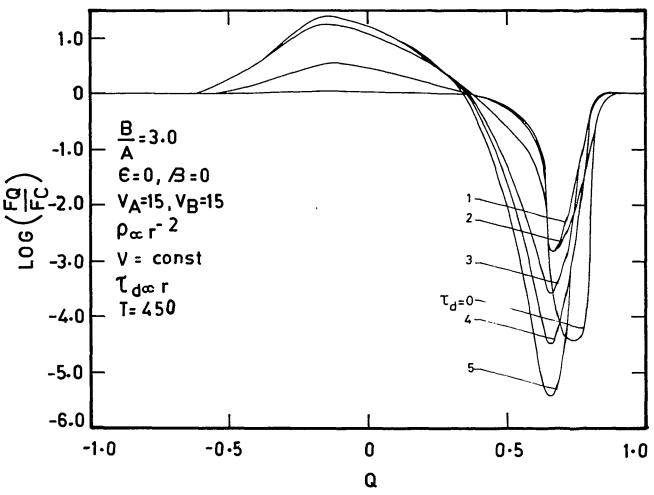

FIGURE 59. — Same as those given in figure 57 but V_B = 15 Doppler units.

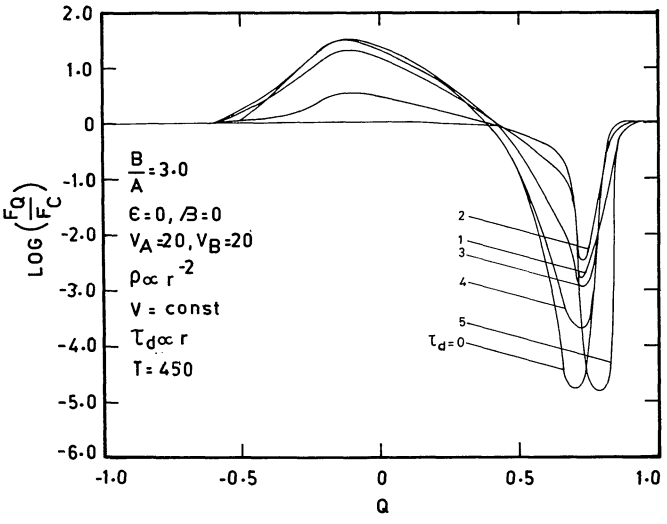

FIGURE 60. — Same as those given in figure 57 but V_B = 20 Doppler units.

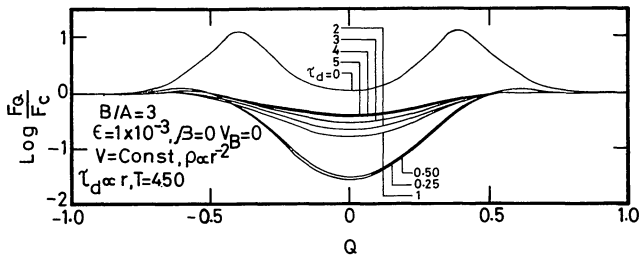

FIGURE 61. — Line profiles formed in a static medium in which dust density increases proportionately with r and the gas density changes as r^{-2}. The total gas optical depth $T = 450$.

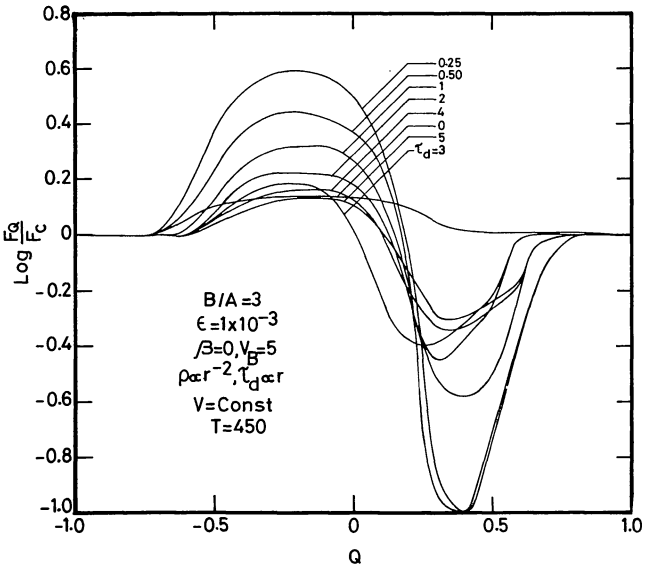

FIGURE 62. — Same as those given in figure 61 but $V_B = 5$ Doppler units. There are no velocity gradients.

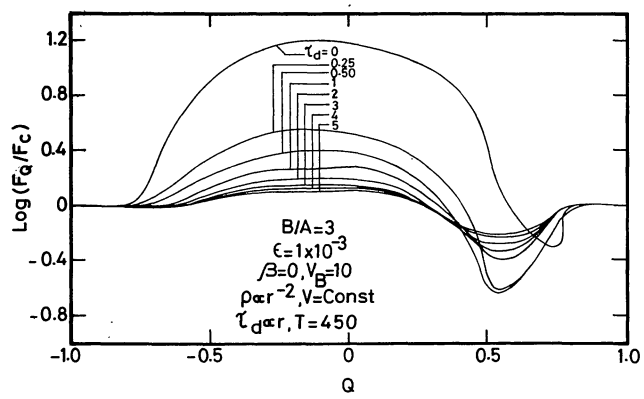

FIGURE 63. — Same as those given in figure 62 but $V_B = 10$ Doppler units.

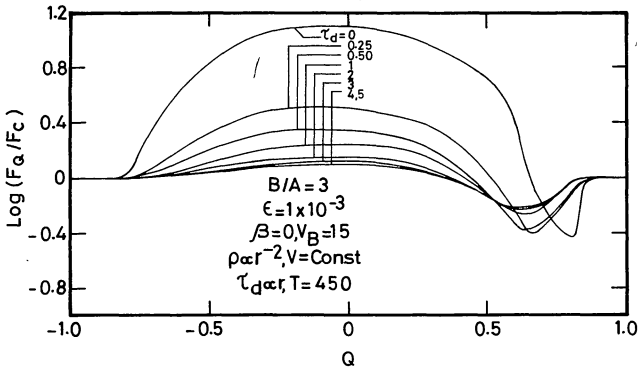

FIGURE 64. — Same as those given in figure 62 but $V_B = 15$ Doppler units.

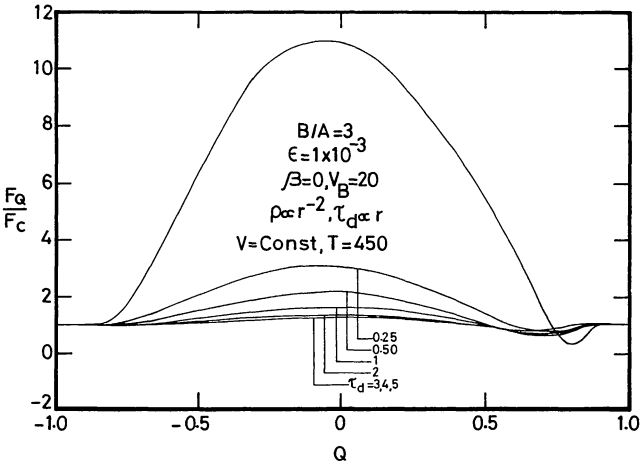

FIGURE 65. — Same as those given in figure 62 but $V_B = 20$ Doppler units.

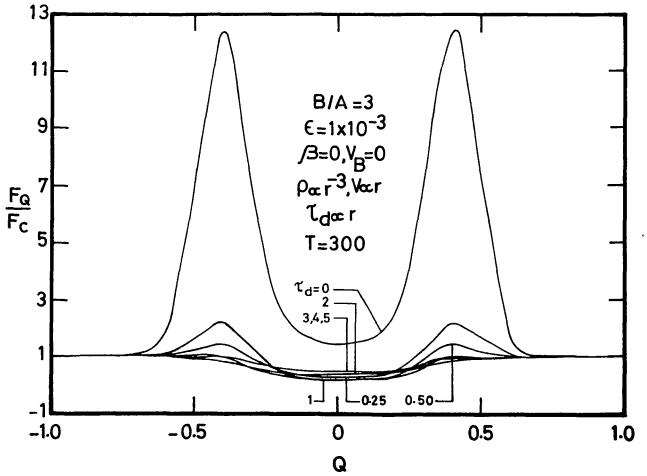

FIGURE 66. — Line profiles formed in static medium with line emission. Dust density increases proportionately with r and the gas density changing as r^{-3}. The total gas optical depth $T = 300$.

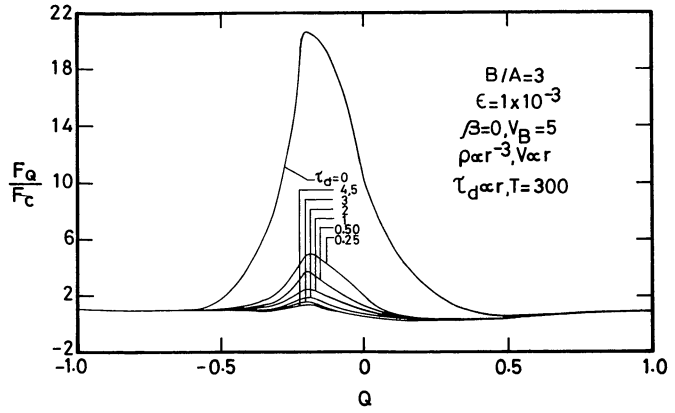

FIGURE 67. — Same as those given in figure 66 but with expanding velocity of $V_B = 5$ Doppler units. The medium is expanding with velocity gradients.

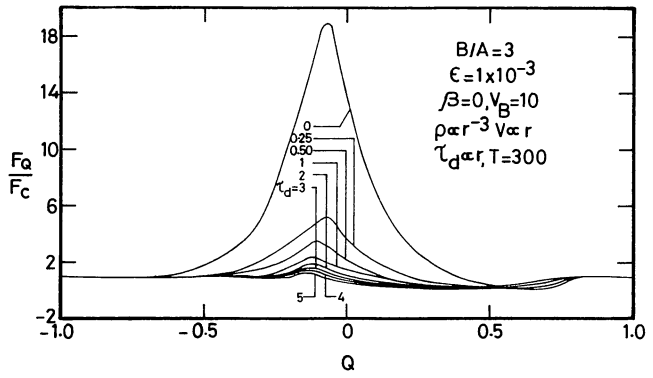

FIGURE 68. — Same as those given in figure 66 but $V_B = 10$ Doppler units.

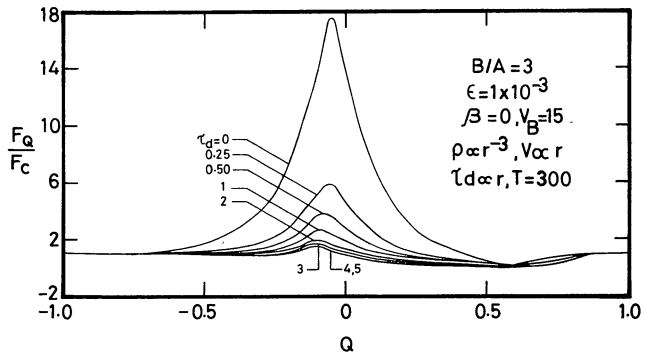

FIGURE 69. — Same as those given in figure 67 but $V_B = 15$ Doppler units.

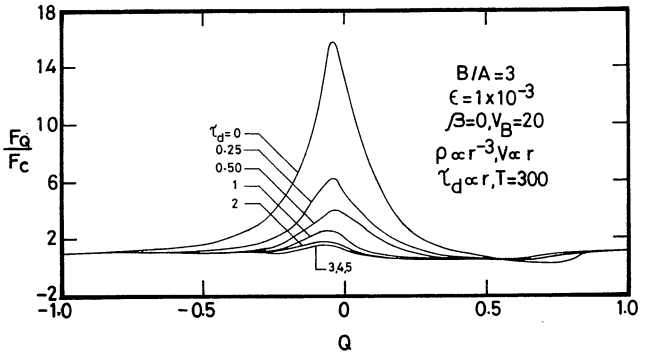

FIGURE 70. — Same as those given in figure 67 but $V_B = 20$ Doppler units.

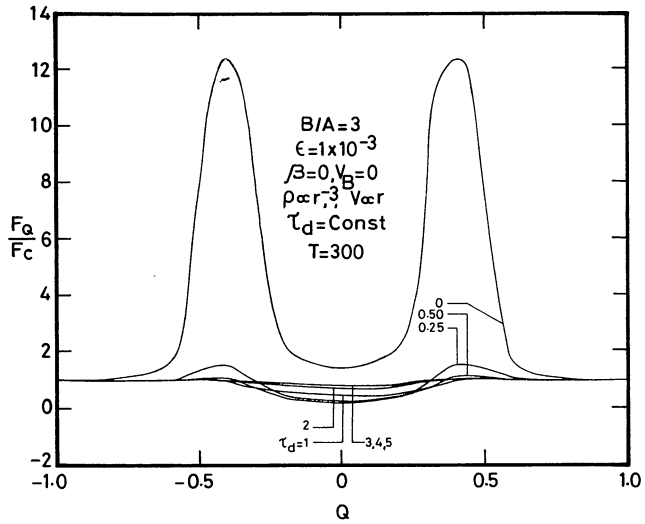

FIGURE 71. — Line profiles formed in static medium with line emission. The dust is distributed uniformly and the gas density is changing as r^{-3}. The total gas optical depth $T = 300$.

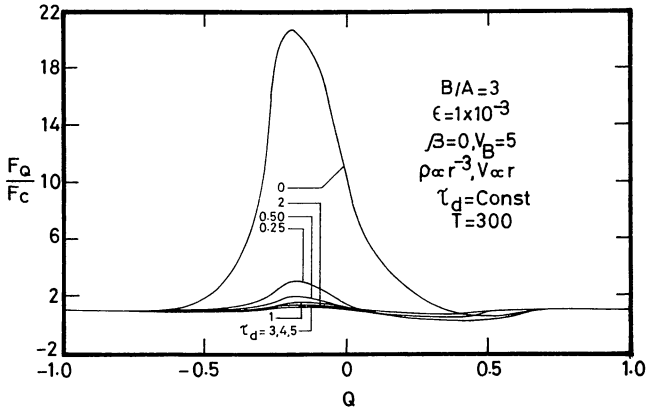

FIGURE 72. — Same as those given in figure 71 but with $V_B = 5$ Doppler units. The medium is expanding with velocity gradients.

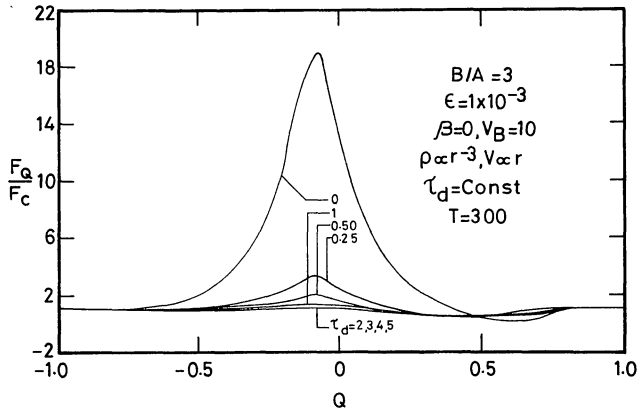

FIGURE 73. — Same as those given in figure 72 with $V_B = 10$ Doppler units.

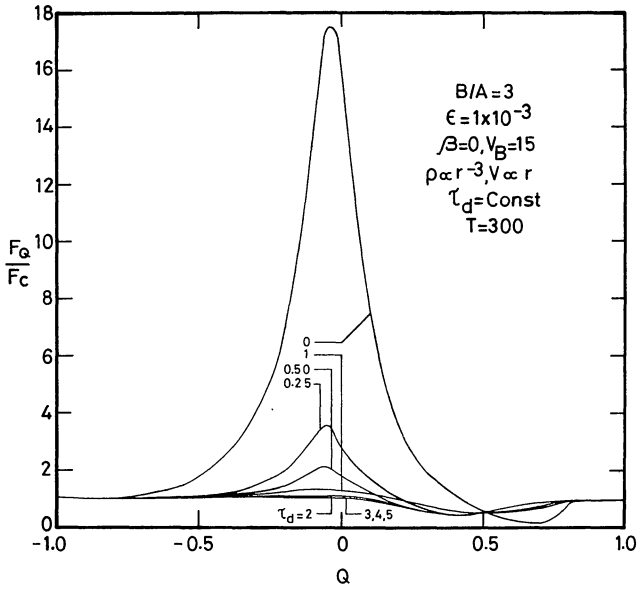

FIGURE 74. — Same as those given in figure 72 but with $V_B = 15$ Doppler units.

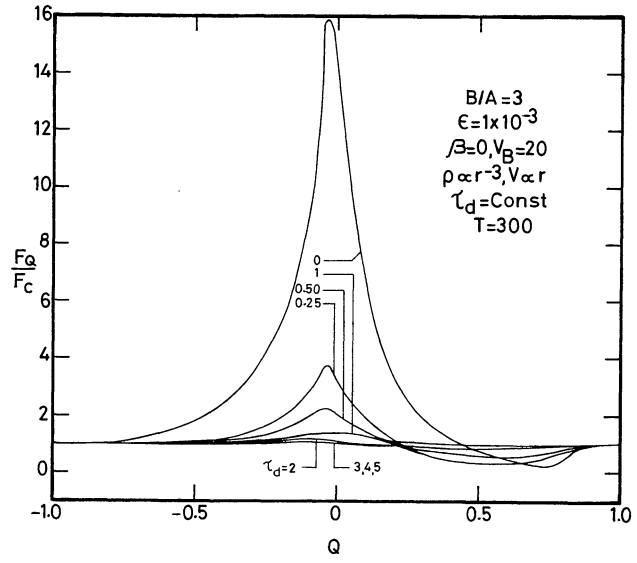

FIGURE 75. — Same as those given in figure 72 with $V_B = 20$ Doppler units.

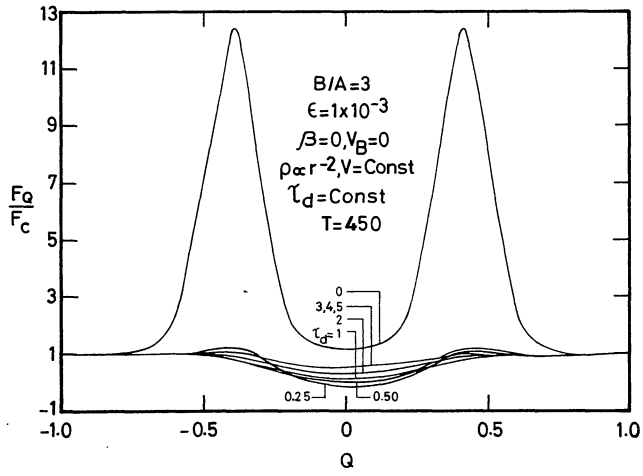

FIGURE 76. — Line profiles formed in a static medium with line emission. The dust is distributed uniformly and the gas density changes as r^{-2}. The total gas optical depth $T = 450$.

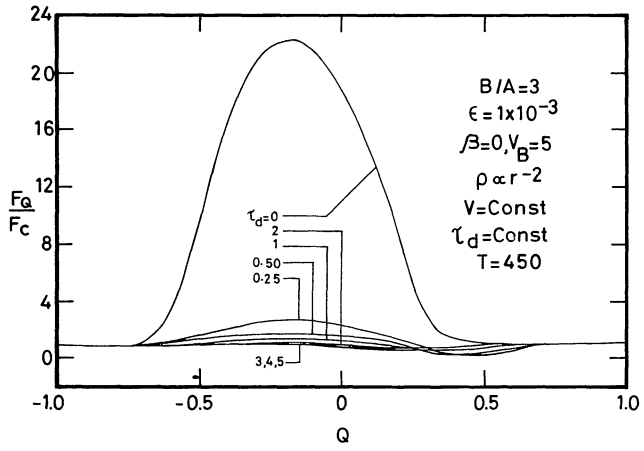

FIGURE 77. — Same as those given in figure 76 but with $V_B = 5$ Doppler units and without velocity gradients.

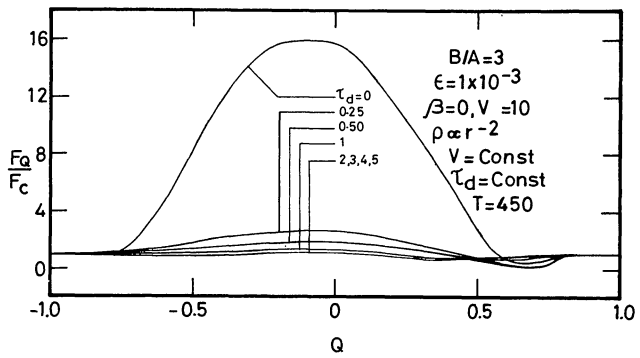

FIGURE 78. — Same as those given in figure 77, but with $V_B = 10$ Doppler units.

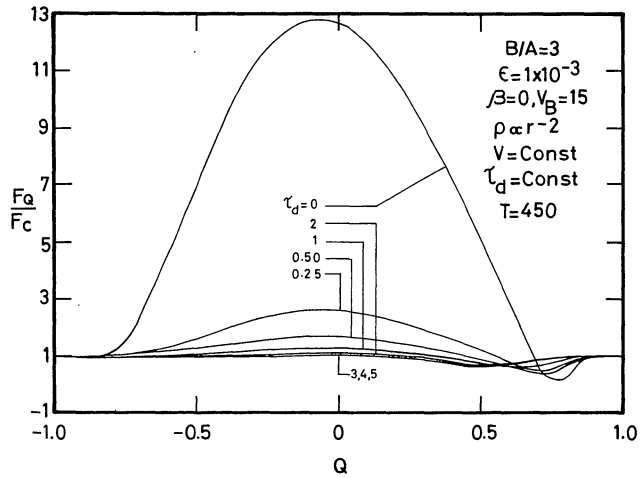

FIGURE 79. — Same as those given in figure 77, but with $V_B = 15$ Doppler units.

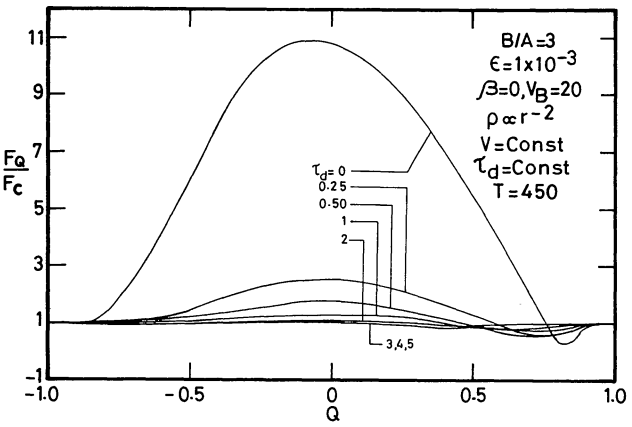

FIGURE 80. — Same as those given in figure 77, but with $V_B = 20$ Doppler units.